Article:
Terzioglu, F. and Rongong, J.A. (2025) Selection of granular damper parameters to achieve optimum vibration attenuation on vibrating structures. Mechanical Systems and Signal Processing, 229. 112512. ISSN: 0888-3270

https://doi.org/10.1016/j.ymssp.2025.112512

Selection of granular damper parameters to achieve optimum vibration attenuation on vibrating structures

Furkan Terzioglu[a] – Corresponding author

Jem Athing Rongong[a]

[a]School of Mechanical, Aerospace and Civil Engineering, University of Sheffield, Mappin Street, Sheffield, S1 3JD, United Kingdom

f.terzioglu@sheffield.ac.uk

j.a.rongong@sheffield.ac.uk

Highlights

- Experimental investigation of optimum granular damping for a vibrating structure
- Presentation of an efficient predictive method for structure-granular damper systems
- Description of the sensitivity of optimum performance to common design parameters
- Detailed study of two different damping processes present in granular dampers leading to potential modelling simplifications

Abstract

This study provides a compact understanding on the factors that influence the non-linear dissipative performance of granular dampers. The work focuses on the two main motion types within the damper: fluidisation and two-sided collective collision. This is accomplished by conducting experiments on a beam with an attached granular damper and by simulating the beam-damper system with a computationally efficient predictive model. The model is validated by comparing results with those from physical experiments. The results demonstrate that damper parameters affect the two motion types in different ways. Current knowledge of damper performance is explained with this view. Remaining uncertainties are investigated and explained using the experimental and numerical approaches. It is shown that the two types of behaviour can be optimised separately from each other, leading to the understanding that existing damper performance charts can be decomposed for damper-level modelling.

Keywords: optimum particle damping, modal damping prediction, particle damper design

1 Introduction

Granular dampers provide a robust, passive method for vibration reduction and noise attenuation in structures. A typical granular (or particle) damper involves a cavity within (or attached to) the host structure that is partially filled with small particles. The key mechanism enabling the vibrational energy dissipation is the momentum exchange that transfers kinetic energy from the host structure to the particles. The energy transmitted to the particles is dissipated through inelastic collisions and friction amongst the particles, and between the particles and the walls of the cavity.

For practical applications, it is desirable to develop a theoretical model that can be used to study damper performance and therefore various approaches for modelling granular dampers have been proposed in the literature. Analytical models have been developed that represent a granular damper as an equivalent single impact damper [1–3] or consider the damping particles as a nonlinear viscous medium utilising multi-phase flow theory [4,5]. However, there is no inclusive analytical model that captures the full range of dynamic behaviour observed [6]. More recently, interest has grown in data-driven metamodels to represent measured behaviours [7–9].

Numerical tools are commonly used for simulating granular dampers as they operate in different vibration regimes [10]. The Discrete Element Method (DEM) [11] is the most common approach as it enables accurate computation of the energy dissipated by the damper itself [12–15]. When the damper is connected to a vibrating structure, the effect on vibration levels has been investigated using coupled simulation with other numerical tools including multi body dynamics [16] and the Finite Element Method (FEM) [17]. These coupled simulations require the transfer of forces and moments, generated by particle interactions with the cavity walls, from DEM to the secondary simulation tools at each time increment. The secondary simulation tools calculate the structural response and excitation conditions at the damper location and deliver them to DEM for the next iteration. Because of this, coupled simulations require large computational effort.

While the advantages of granular dampers are widely mentioned in the literature [18–22], their practical implementation requires the consideration of many factors that affect performance [23–26]. It is recognised that granular dampers exhibit significant non-linearity with respect to vibration amplitude and frequency [27,28] that is defined by the motional phase (the collective motion of the particles experiencing vibration). A change in the

motional phase alters the direction, magnitude and quantity of individual contact interactions within the cavity which in turn can significantly alter the overall momentum exchange and energy dissipation. Other parameters that affect the motional phase include the volume fill ratio [29], particle shape [30,31], existence or lack of gravity [32–34] and gravity-to-vibration orientation [24].

This paper aims to simplify the design process involved with practical implementation of granular dampers in engineering structures. This is achieved by providing a compact explanation of factors that control the performance of granular dampers and an efficient simulation approach for predicting their effectiveness in reducing structural vibration that is consistent with the capabilities of standard commercial software. It should be noted that this work utilises a mode-based approach, focusing particularly on single-harmonic excitations around resonant frequencies.

2 Problem description

Many different motional phases have been identified [29,35,36] and efforts made to understand how the motional phase relates to energy dissipation [24,25,29,32,34,37]. These studies either focus on individual motional phases that can be observed under specific conditions [26,29,37,38] or attempt to map the changes in motional phase over a broad range of conditions [24,25].

Regardless of the excitation-to-gravity orientation, the dissipative-based motional behaviours of particles can be categorised in two distinct motional mechanisms in granular dampers: the collective collision and the solid-fluidisation-convection phase transitional process [24,39]. Figure 1 briefly illustrates some of the important particle motions.

The collective collision is where particles form a compact medium and collide with a wall of the damper cavity (often perpendicular to the direction of excitation). This is the most fundamental motion type for conventional granular dampers (as opposed to strain-based granular dampers [40]) and is highly efficient in transferring energy to the particles. Significant relative motions are observed within the granular medium as collective collision occurs. If the collective collision occurs at both ends of the cavity within one vibration cycle, the particles cannot find enough time to de-compact from each other. This condition is referred to as two-sided collective collision or bouncing bed. It has been shown

[24,25,30,32,33] that the enclosure acceleration amplitude that initiates the two-sided collective collision, $\ddot{u}_c$, depends on the damper clearance, $h_{\text{clearance}}$, according to:

$$\ddot{u}_c = \omega_e^2 h_{\text{clearance}} / \pi \tag{1}$$

where ω_e is the excitation frequency in rad/s, and the damper clearance can be approximated as:

$$h_{\text{clearance}} = L_{\text{enclosure}} \left(1 - \upsilon / \upsilon_{\max}\right) \tag{2}$$

where $L_{\text{enclosure}}$ is the length of enclosure in the direction of the excitation, υ is the volume fill ratio by particles and $\upsilon_{\max}$ is the maximum volume fill ratio that can be achieved in the damper cavity ranging between 0.55-0.64 for a randomly packed particle arrangement [41,42].

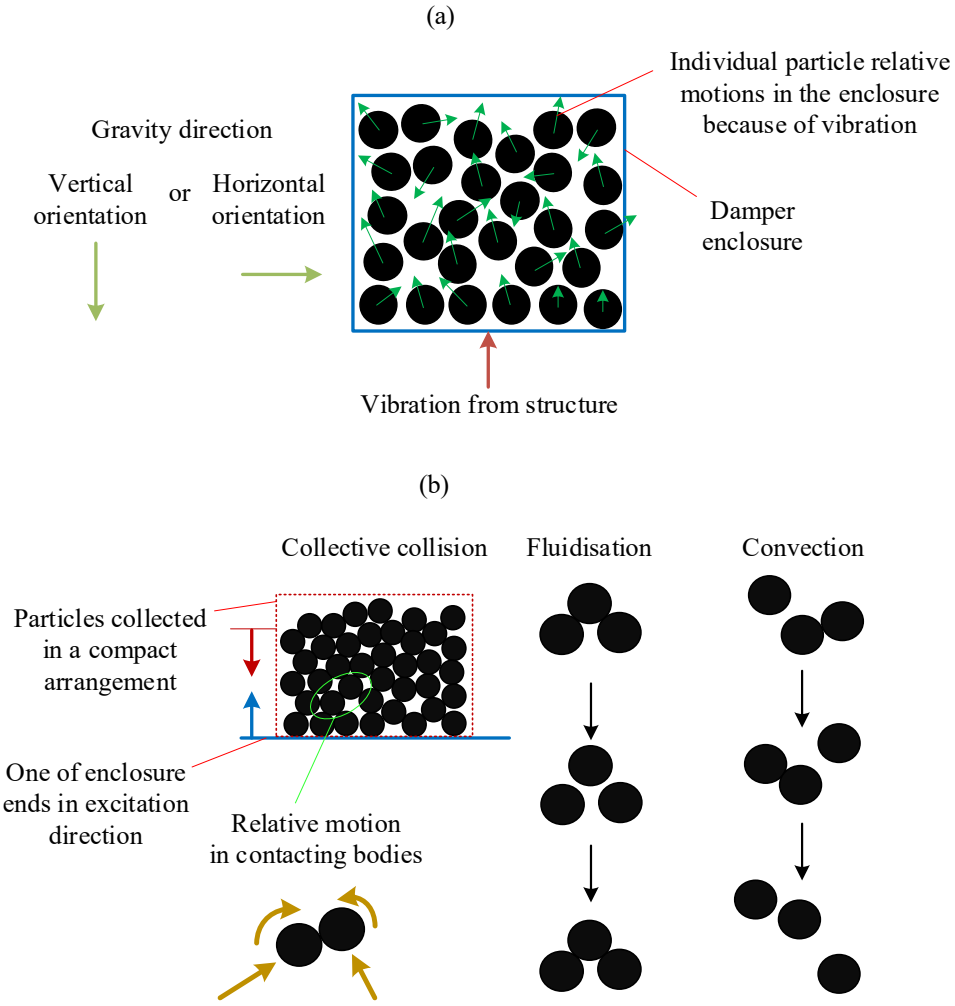

Figure 1: Motional analogy in granular dampers: (a) individual particle motional behaviour, (b) dissipation-based fundamental particle motions.

The solid-fluidisation-convection process occurs where gravity is present. The solid condition is generally observed at vibration levels smaller than unit gravity where there is no collective collision with the cavity walls so particles do not move relative to the damper enclosure. At higher amplitudes, the granular medium lifts away from the enclosure and falls under the influence of gravity for part of a vibration cycle. The remaining part of the cycle involves a collective collision with the floor of the enclosure. This process causes the particles to de-compact and, depending on the amplitude, two principal behaviours known as particle 'fluidisation' and 'convection' are observed [25,29,35]. When fluidised, particles temporarily lose contact and move relative to each other but, over a vibration cycle, approximately retain their average position and existing contacts. At higher excitation levels, convection motion occurs where particles move to different locations and lose their existing contacts over a vibration cycle.

In the studies which investigate the relation between granular motional behaviour and energy dissipation [24,25,29,32,34,37], useful non-dimensional parameters are the energy dissipation effectiveness (ϵ) and the gravity-normalised vibration acceleration amplitude (Γ). If the acceleration of the enclosure is $\ddot{u}$, the non-dimensional amplitude is,

$$\Gamma = \ddot{u} / g \tag{3}$$

where g is gravitational acceleration. The dissipation effectiveness, defined as the ratio of the energy dissipated per cycle ($\tilde{E}_{\text{dissipated}}$) due to inter-particle and particle-cavity wall friction and inelastic collisions during steady-state vibrations, to the maximum energy ($\tilde{E}_{\text{dissipated,max}}$) dissipated by an ideal impact damper where the impactor mass equals the total particle mass (m) is given by,

$$\epsilon = \tilde{E}_{\text{dissipated}} / \tilde{E}_{\text{dissipated,max}} \tag{4}$$

It should be noted that the dissipation of the ideal impact damper is based on completely inelastic impacts with both cavity end walls when the enclosure reaches peak velocity and the impactor has an equal and opposite velocity [32],

$$\tilde{E}_{\text{dissipated,max}} = 4\left(\Gamma g / \omega_e\right)^2 m \tag{5}$$

The two distinct motional mechanisms described above (the collective collision and the solid-fluidisation-convection process) are frequently recognised as being important in terms of

granular energy dissipation [24,30]. Each has its own optimum, which can be identified on a plot of energy dissipation effectiveness against vibration amplitude, as shown in Figure 2.

The first peak shown in Figure 2, that occurs at amplitude Γ_f, relates to the solid-fluidisation-convection phase transition process. This "fluidisation optimum" is achieved when increases in dissipation from rising intensity of relative motion between particles is balanced by decreases in dissipation from reduced contact due to decompaction.

The second (and higher) peak, that occurs at amplitude Γ_c, is defined as the "two-sided collective collision optimum". In this condition, all the particles move together and collide with the ends of the cavity at points in the cycle that create maximum dissipation.

Both motion types associated with optimum performance have received considerable attention over the years. Each responds differently to changes in parameters and often only one is observable, particularly if the excitation amplitude and frequency range is narrow. This is one of the main causes for seemingly inconsistent results being reported and the resulting lack of consensus on a robust design methodology. To help address this, the current knowledge about the sensitivity of each peak (specifically, the optimum dissipation effectiveness and the amplitude at which it occurs) to the main damper design parameters is summarised in Table 1. Note that the use of dissipation effectiveness pre-supposes the widely held view that the maximum energy dissipation achievable is directly proportional to the mass of particles present – as indicated in Equation (5).

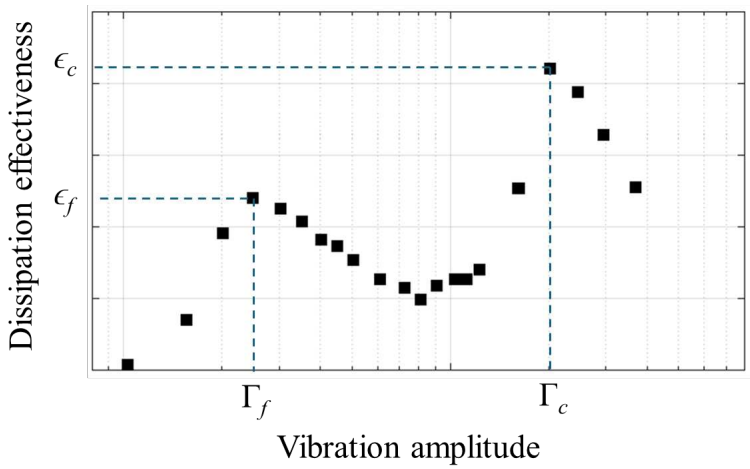

Figure 2: Typical sensitivity of granular dissipation effectiveness to excitation amplitude. (experimental data obtained from sinusoidal excitation of a cylindrical damper [24])

A designer seeking to reduce vibration levels on a structure using a granular damper must decide on the points listed below.

1. *The desired system performance*. Usually defined as a reduction in vibration amplitude under specific conditions, ideally using natural frequency and modal damping information for selected resonances without and with the application of the damping system.
2. *The mass of particles to use and their location on the structure*. A damper usually has greatest effect if it is located at the point on the structure where the motion is highest. Damping increases with the mass of particles used, but large increases in system mass are not often acceptable.
3. *The type of granular motion to utilise*. The intensity and variability of the vibrations under consideration will tend to define whether the fluidisation or two-sided collective collision is the most suitable option.
4. *The detailed design of the damper*. This focuses on the definition of the enclosure size and shape along with the particle details including size, material and contact properties.

The information summarised in Table 1 provides a guidance on Points 3 and 4, although it is noticeable that the effects of some parameters remain uncertain. The supporting detailed analysis can be carried out either via DEM or damper-only experiments. To achieve Points 1 and 2 however, it is likely that a modal analysis of the structure itself is necessary, either via FEM or experiment. Thus, to enable informed design, linked analyses involving structure-level and damper-level models is necessary.

Table 1: Current understanding of factors affecting the optimum points on the effectiveness-amplitude plot related to the two principal motional mechanisms.

Factor	Property	Fluidisation		Two-sided collective collision	
		Location, Γ_f	**Height, ϵ_f**	**Location, Γ_c**	**Height, ϵ_c**
Excitation	Frequency	Uncertain, but reduces slightly as frequency increases [24,28,43,44]	Uncertain, but appears to increase at low frequency [24,28,45]	Linearly proportional to the square of frequency [24,25,30,32,33,46]	Not affected [24,30,32]
	Gravity presence	Requires gravity to exist [24,33,34]	Requires gravity to exist [24,33,34]	Not affected [24,25,30,33,34,46]	Not affected [24,30]
	Orientation with respect to gravity	Not affected [24,33,34]	Not affected [24–26]	Not affected [24,25,30,33,34,46]	Not affected [24,30]
Collection of particles	Clearance	Not affected [24,25,30,39,43]	Not affected [24,25,30,39,43]	Linearly proportional to clearance [24,25,30,32,33,39]	Not affected [24,25,30,32,33,39]
	Bed depth	Higher with increasing bed depth [27,28,44,47]	Not affected [27,28,44,47]	Only if it alters the clearance [24,25,30,32,33,39]	Not affected [24,25,30,32,33,39]
	Shear resistance	Not mentioned	Not mentioned	Higher with increasing shear resistance [30]	Not affected [30]
Individual particle	Density	Slightly lower with increasing density [22,48,49]	Not affected (but note that this alters the total mass) [24,48–50]	Not affected [30]	Not affected (but note that this alters the total mass) [24,25,30,32,33,50]
	Size	Not affected [24,50]	Not affected [24,50]	Only if size alters effective clearance [24,50]	Not affected [24,50]
	Elastic modulus	Uncertain	Slightly lower with increasing modulus [51]	Uncertain, but tends to rise with increasing modulus [30]	Uncertain
	Coefficient of Restitution (COR)	Not affected [22,49,51,52]	Slightly higher with increasing COR [22,49,51,52]	Uncertain, but does not seem to be affected [30]	Slightly higher with increasing COR [30]
	Coefficient of Friction (COF)	Inconsistent results [22,48,49,51,52]	Inconsistent results [22,48,49,51,52]	Inconsistent results [22,30,48,49,51,52]	Inconsistent results [22,30,48,49,51,52]
	Sphericity	Uncertain but appears to have no effect [53]	Uncertain but appears to have no effect [53]	Higher with decreasing sphericity (due to change in shear resistance) [30,31]	Not affected [30,31]

This paper presents an efficient approach that enables all four points above to be addressed. Section 2 describes a simple process for predicting the modal damping of a structure when a granular damper is attached to it. This approach is validated using controlled experiments for several vibration modes of a beam. Section 3 provides clarification on the effects of damper parameters that are considered uncertain or missing in Table 1. This is achieved through various combinations of experiment and numerical analysis. In this way, previous understanding and new results are tied together to provide an accurate, efficient and comprehensive way to design and optimise granular dampers. It is important to note that this work focuses on situations where the vibration is primarily in one direction.

3 Estimation of the modal damping of a structure incorporating a granular damper

This section develops an efficient numerical approach that links the steady-state vibration response of a structure incorporating granular dampers to the design parameters of the damper itself. The underlying assumption is that the damped vibration modes of the structure can be approximated by the real mode shapes. It is shown in Appendix A that this is a reasonable estimation because the resulting errors associated with this estimation are small for typical granular dampers. Hence a simple linear natural frequency extraction routine in FEM can be used in conjunction with damper-only analyses in DEM.

3.1 Analysis method

FEM discretises a continuous structure into small elements whose strain-stress relations at each degree-of-freedom are determined based on the elasticity theories [54]. Natural frequency (ω) and mode shape (ϕ) information can be obtained by solving an eigenvalue problem involving the stiffness matrix ([K]) and the mass matrix ([M]) whose dimensions are equal to the number of degrees-of-freedom in the spatially discretised model.

Conventionally, the damping ratio at a vibration mode of a structure can be described as [55]:

$$\zeta_r = \tilde{E}_{\text{dissipated},r} / \left(4\pi E_{\text{strain},r}\right) \tag{6}$$

where $\tilde{E}_{\text{dissipated},r}$ is the total energy dissipated over a vibration cycle at the frequency of the mode r and $E_{\text{strain},r}$ is the maximum strain energy that is stored in the structure considered within this vibration cycle. Equation (6) can be used to predict the damping ratios of structures enriched with granular dampers. However, to achieve this, the energy terms ($E_{\text{strain},r}$ and $\tilde{E}_{\text{dissipated},r}$) need to be evaluated.

Following the eigenvalue extraction routine to obtain the natural modes, $E_{\text{strain},r}$ can be determined as:

$$E_{\text{strain},r} = \left(1/2\right)\{x\}_r^{\mathrm{T}}\left[\mathrm{K}\right]\{x\}_r \tag{7}$$

where $\{x\}_r$ is the maximum displacement vector of the structure as it vibrates at mode r and the superscript T represents the mathematical transpose. For a linear model, the maximum displacement vector can be represented using the modal properties as:

$$\{x\}_r = \gamma_r \{\phi\}_r \tag{8}$$

where $\{\phi\}_r$ is the mass normalised shape of mode r, obtained by performing an eigen-solution of the model. The coefficient γ_r is a scaling factor for the mode shape of interest, which can be determined by considering the degree-of-freedom of the structure (identified by i) where the external excitation conditions are defined.

$$\gamma_r = x_r^{(i)} / \phi_r^{(i)} \tag{9}$$

Substituting Equation (8) into Equation (7), $E_{\text{strain},r}$ becomes:

$$E_{\text{strain},r} = (1/2)\gamma_r^2 \{\phi\}_r^{\mathrm{T}} [\mathrm{K}] \{\phi\}_r \tag{10}$$

As a result of the orthogonality, for mass-normalised modes $\{\phi\}_r^{\mathrm{T}}[\mathrm{K}]\{\phi\}_r = \omega_r^2$ where ω_r is the frequency of mode r in rad/s. Thus, Equation (10) becomes:

$$E_{\text{strain},r} = (1/2)\gamma_r^2 \omega_r^2 \tag{11}$$

The other energy term in Equation (6), $\tilde{E}_{\text{dissipated},r}$ can be predicted by employing a DEM model of the granular damper and subjecting it to vibrations at the frequency of mode r. DEM is a time-marching numerical computational method to model the dynamics of granular assemblies [56]. It considers each particle as a distinct body, so that particles can move independently within the model space during a simulation history. This is unlike a continuum approach where movement is defined by local strains which are related to loading by using constitutive equations.

In DEM simulations of granular dampers, at each simulation time step, the excitation (time-dependent force or motion) is usually applied to the walls of the cavity that encloses the particles. The forces acting on each particle, arising from interactions between particles and between particles and the walls, are computed based on the contact theories used [57]. Newton-Euler equations of motions are constructed for all particles using the resultant forces acting on them. By numerically integrating the equations of motions, both positions and rotations of each particle are evaluated. A DEM simulation history is constructed by solving the equations at successive points in time. The time step needs to be small enough to capture individual contact durations so that individual contact forces are represented accurately. DEM has been shown to be a reliable method for simulating the energy dissipation of granular dampers in the literature [12,13,51,58–61].

As DEM is a time-discretised method, the energy dissipated over a period of time should be calculated by summing the energy dissipated over each time step. Thus, the total energy dissipated from the beginning of a simulation ($t = 0$) to an arbitrary time, t, is computed as:

$$E_{\text{dissipated}}\left(t\right) = \sum_{s=1}^{t/\Delta t} \Delta E_{\text{dissipated}}\left(t_s = s\Delta t\right) \tag{12}$$

where Δt is the time step and t_s represents the time points at the end of each time step.

For a typical granular damper, the energy dissipation only arises from contact forces, and thus in each time step, $\Delta E_{\text{dissipated}}$, is obtained considering all particles and contacts:

$$\Delta E_{\text{dissipated}}\left(t_s\right) = \sum_{i=1}^{N_{\text{particle}}} \sum_{j=1}^{N_{\text{contact},i}\left(t_s\right)} \left\{ {F_{\text{contact},ij}}^{nd}\left(t_s\right) {v_{\text{rel},ij}}^{n}\left(t_s\right) + {F_{\text{contact},ij}}^{td}\left(t_s\right) {v_{\text{rel},ij}}^{t}\left(t_s\right) \right\} \Delta t \tag{13}$$

where N_{particle} is the total number of particles in the simulation, $N_{\text{contact},i}$ is the total number of contacts that the particle i has at the time point considered, ${F_{\text{contact},ij}}^{nd}$ and ${F_{\text{contact},ij}}^{td}$ are respectively the dissipative components of contact forces along normal and tangential directions at the same simulation time point, ${v_{\text{rel},ij}}^{n}$ and ${v_{\text{rel},ij}}^{t}$ are the relative velocities along normal and tangential directions at the same time point, respectively. If there are significant internal losses in the particles, Equation (13) will contain extra terms, but the analysis process remains the same.

Because of the relatively random arrangement of particles in a granular system, the energy dissipated over a cycle differs from one vibration cycle to another even for nominally steady-state oscillation. Therefore, a more reliable estimate of the energy dissipated can be obtained by averaging over several cycles. This can be formulated as:

$$\tilde{E}_{\text{dissipated}} = \frac{E_{\text{dissipated}}\left(t_{\text{initial}}\right) - E_{\text{dissipated}}\left(t_{\text{final}}\right)}{t_{\text{final}} - t_{\text{initial}}} \frac{2\pi}{\omega_r} \tag{14}$$

where t_{initial} and t_{final} are respectively the time points at which the steady-state vibration begins and the time at which the simulation ends.

3.2 Method validation

This section describes a test case that was evaluated using the new method and validated by comparison with physical experiments.

3.2.1 Structure and damper design parameters

The structure considered was a steel beam of cross section 4 mm × 20 mm that was clamped at both ends leaving an effective length between clamps of 580 mm. The granular damper was attached rigidly to the centre of the beam as indicated in Figure 3.

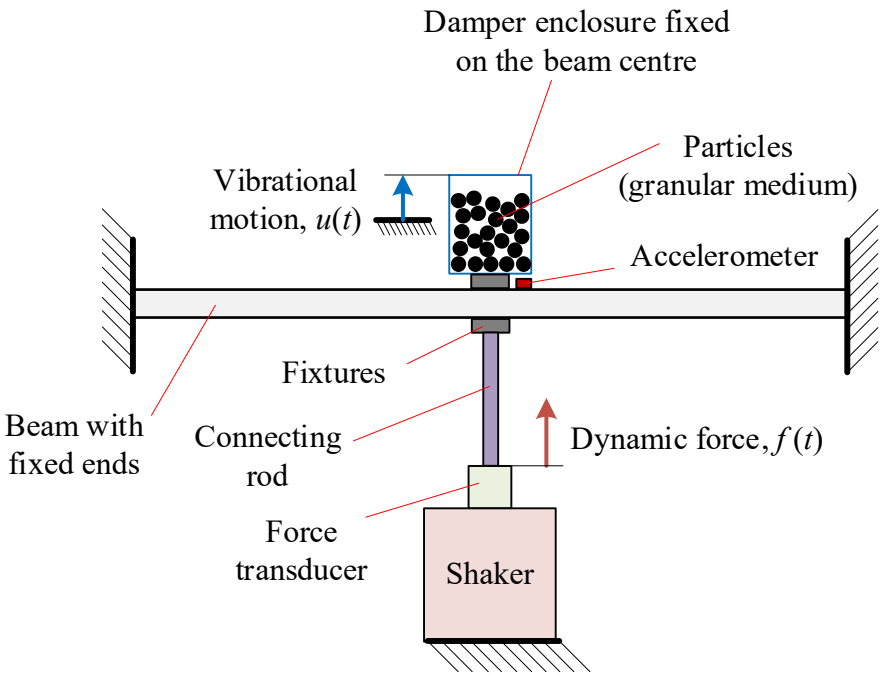

Figure 3: Arrangement of the beam with the granular damper.

The damper enclosure had a cylindrical cavity whose diameter and height were both 40 mm and its typical wall thickness was 4 mm. To observe particle motions, the enclosure was made from polymethyl methacrylate (PMMA) which is transparent. Sinusoidal excitation was applied perpendicular to the beam, in line with the axis of the damper, via a connecting rod. The mass of the enclosure, fixtures and connecting rod was 0.200 kg. Note that the enclosure was considered rigid as its first natural frequency was found to be well above the vibration modes of interest for the beam. The enclosure contained 120 particles made from PMMA with radius 3.73 mm.

Comparisons between predictions and measurements were made for flexural modes 1, 3 and 5 because these mode shapes are known from theory to be symmetric, ensuring that the centre-mounted damper experiences motion in translation rather than rotation. The vibration amplitude range for the study was set as $\Gamma = 0.1\text{-}15$, measured at the damper connection point.

3.2.2 Numerical model

The approach described in Section 2.1 is summarised in Figure 4.

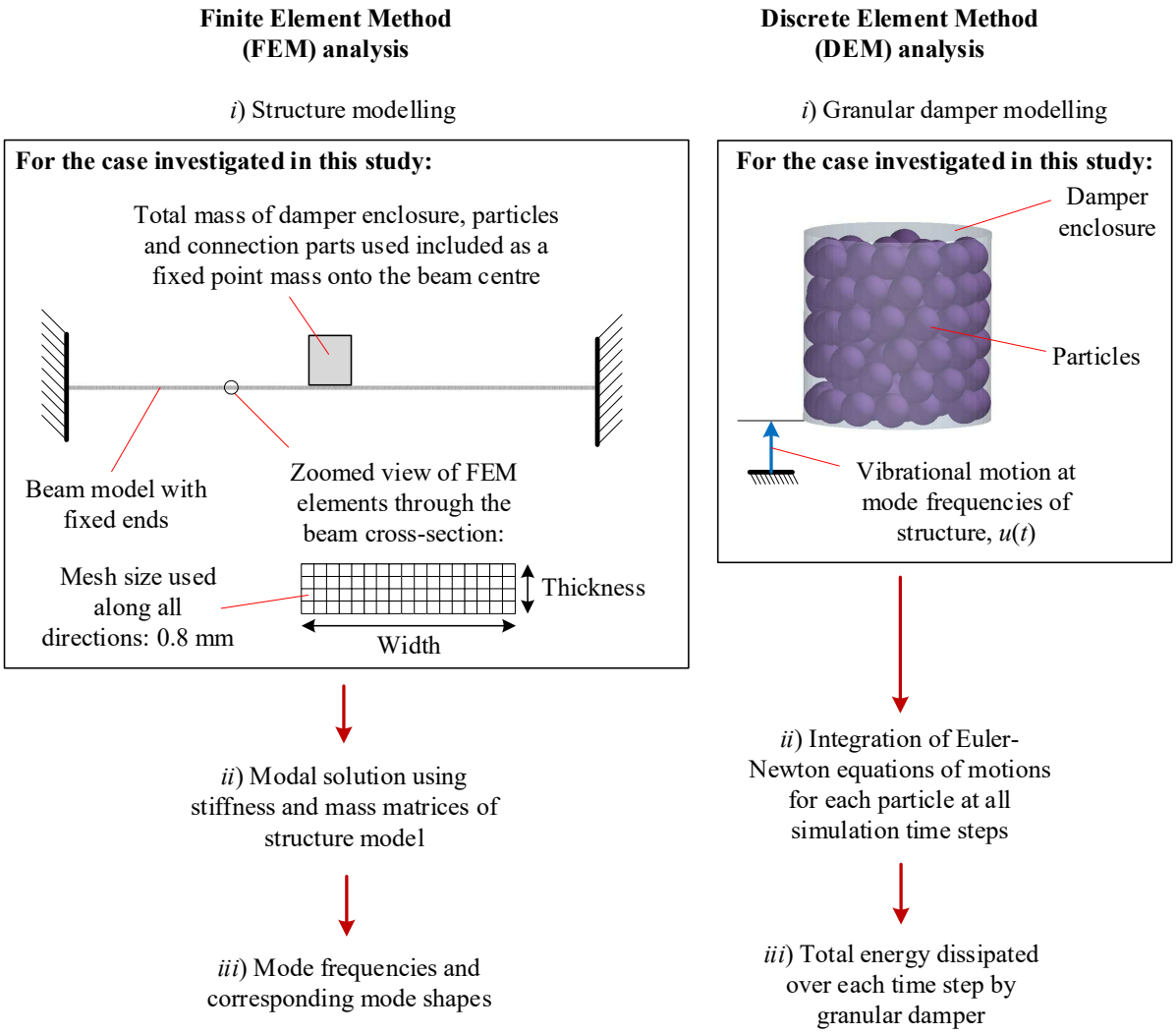

Figure 4: Damping prediction workflow for a structure enriched with a granular damper (the damping at each mode is obtained from Equation (6)).

The FEM model of the beam included the granular damper and associated connectors. The beam was discretised using standard three-dimensional quadratic brick elements in a commercial FEM package [62]. The material properties used for the beam are provided in Table 2. The damper and connectors were assumed to add no stiffness to the system and therefore modelled as a point mass at the centre of the beam.

The DEM analysis was conducted using commercial DEM software [63]. The damper enclosure was modelled as a cylindrical rigid cavity. Material and contact information is provided in Table 2. The simulation time step used was 2×10^{-6} seconds. The particles were randomly generated within the cavity and allowed to settle by the effect of gravity. The duration of this particle packing process was 0.2 seconds. The vibrational excitation was applied to the damper enclosure as the time-dependent sinusoidal signals. The excitation

frequencies were the mode frequencies obtained from the FEM model while the amplitudes were defined by the range $\Gamma = 0.1\text{-}15$. Each excitation condition (i.e., a frequency and amplitude pair) were simulated for 0.3 seconds to obtain the steady-state results over many cycles.

Table 2: Material properties used in simulations.

Material	**Property**	**Unit**	**Value**
Steel (used in FEM)	Density	kg/m^3	7800
	Young's modulus	GPa	210
	Poisson's ratio	-	0.3
PMMA (used in DEM)	Density	kg/m^3	920
	Young's modulus	GPa	3.3
	Poisson's ratio	-	0.37
	COR	-	0.52
	COF	-	0.86

In the DEM model, it was assumed that the contact forces were generated by inelastic collisions between the bodies (i.e., particles and cavity walls) and slipping of these bodies on each other. The built-in non-linear Hertz-Mindlin contact model with the Coulomb friction model was employed between contacts to calculate the elastic and frictional components of the contact forces [64]. The inelastic components of the collisional forces were represented by a viscous dashpot whose damping coefficient was defined by the COR [11].

3.2.3 Experimental approach

While the general layout for the experiment matched with the sketch shown in Figure 3 details of the fixtures for attaching the damper to the beam are provided in greater detail in Figure 5. The fixtures also helped to couple the beam and the electrodynamic shaker via a connecting rod to generate axial vibrations on the damper position. A force transducer was connected between the connecting rod and the shaker to measure the force exerted as the beam underwent vibrations. An accelerometer was bonded next to the centre of the beam to measure vibrational motions.

In this test rig, a controller was used to provide sinusoidal excitations at specific amplitudes and frequencies. The excitation acceleration function was generated via a personal computer and received by the controller which sent this function to a power amplifier to create vibrations in the shaker. The controller achieved the excitation function provided by acquiring the acceleration signal from the accelerometer as the reference – i.e., a feedback loop based on the target and achieved levels. As the system operated, the accelerometer and the force transducer collected the analogue data, and these were conditioned by the help of a

signal conditioner and an oscilloscope analyser. The acceleration and force signals were then converted to the acceleration, $\ddot{u}(t)$ and the force, $f(t)$ using the transducer sensitivities where t depicts the time. These were stored in a second personal computer for further processing.

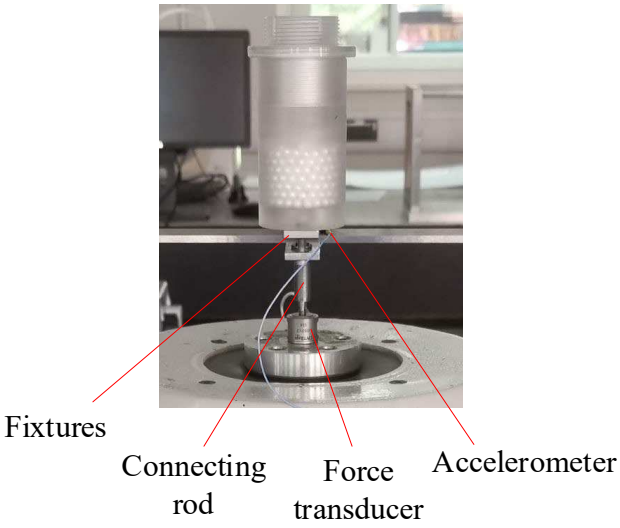

Figure 5: A picture of the experimental setup showing the damper-beam-shaker connection and the positions of the transducers.

The time domain results were transformed into the frequency domain to generate a frequency response function (FRF). To evaluate the damper performance, the point (accelerance) FRFs were computed at desired frequencies using the time-domain signals, $\ddot{u}$ and f:

$$\boldsymbol{\alpha}\left(\omega_{\text{discrete},k}\right) = \mathbf{A}_k / \mathbf{F}_k \tag{15}$$

where $\mathbf{F}_k$ is the complex force at the frequency point k, $\mathbf{A}_k$ is the complex acceleration at the same frequency point and $\omega_{\text{discrete},k}$ is the kth discretised frequency point in rad/s. These frequency-domain force and acceleration data were obtained by applying the discrete Fourier transform for the time-domain signals measured as:

$$\mathbf{F}_k = \sum_{i=0}^{N-1} f\left(t_i\right) e^{-\mathrm{j}2\pi ki/N} \tag{16}$$

$$\mathbf{A}_k = \sum_{i=0}^{N-1} \ddot{u}\left(t_i\right) e^{-\mathrm{j}2\pi ki/N} \tag{17}$$

where N is the total number of discrete time data points determined by the sampling frequency and length of a measurement.

Verification of the experimental process included running repeat tests which showed that natural frequency varied by less than 0.05%. Modal damping ratios were estimated using a

MATLAB algorithm based on the line-fit method [65]. The typical quality of fit is shown in Figure 6.

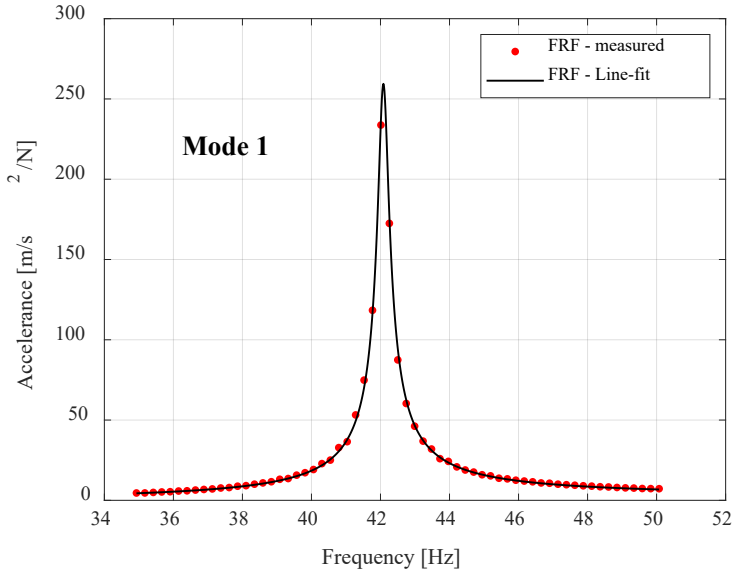

Figure 6: Measured FRF of the beam with empty enclosure around the first mode frequency and generated fit.

3.2.4 Validation of the FEM model using the beam with the empty damper enclosure

The first validation step involved comparing simulated and measured results for the system without particles. The model included a point mass attached at the centre of the beam that represented the inertia of the empty enclosure and attachments.

Experimental results for comparison, were obtained at a vibration amplitude of $\Gamma = 2$. Additional tests were also carried out at a higher level ($\Gamma = 8$) to understand the sensitivity of the results to amplitude from possible microslip at the clamps and fixtures.. The r^{th} mode frequencies in Hz, damping ratios (ζ_r) and mode shapes are shown in Figure 7. Note that the mode shapes of the beam are different from a usual fixed-fixed beam due to the mass attached at its centre.

	Experimental				Numerical – FEM	
	Γ = 2		Γ = 8			
Flexural vibration mode no, r	**Mode frequency, $\omega_r/2\pi$**	**Damping ratio, ζ_r**	**Mode frequency, $\omega_r/2\pi$**	**Damping ratio, ζ_r**	**Mode frequency, $\omega_r/2\pi$**	**Mode shape, ϕ_r**
1	42.0 Hz	0.20%	41.8 Hz	0.33%	40.0 Hz	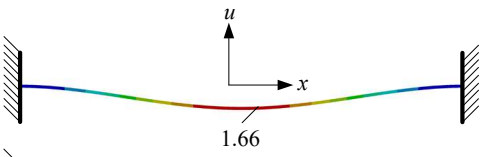
3	268.0 Hz	0.07%	267.5 Hz	0.09%	281.0 Hz	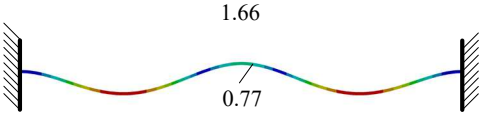
5	687.0 Hz	0.09%	685.8 Hz	0.13%	733.0 Hz	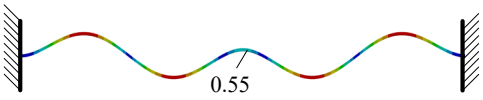

Figure 7: Flexural vibration modes of the beam with the empty damper enclosure.

3.2.5 Experimental results for the beam-granular damper system

For the system incorporating particles in the enclosure, FRFs covering the frequency range close to the first mode are shown in Figure 8a and Figure 8b for various vibration amplitudes. These plots show amplitude dependent behaviour similar to that seen previously [27] where the presence of the particles causes both a reduction in the peak magnitude and a shift in the natural frequency.

The corresponding damping ratio and natural frequency for each vibration amplitude are shown in Figure 8c and Figure 8d, respectively. Results when the enclosure was empty at Γ = 2 and Γ = 8 are also added for comparison.

Figure 8c shows that the granular damper exhibits different dissipative characteristics depending on the vibration amplitude whilst it considerably increases the level of damping compared to the beam with the empty enclosure. At the lowest vibration amplitudes tested (Γ = 0.5-1), the damping ratio is low, corresponding to what might be expected in the solid phase. If the amplitude is increased, there is a significant rise reaching a peak between Γ = 2 and Γ = 4. Observation of the particles during testing indicated that this corresponds to the fluidisation optimum, Γ_f. Further increases in amplitude result in a second (higher) peak near Γ = 6, corresponding to the two-sided collective collision optimum Γ_c, followed by a gradual decline for Γ > 6. Figure 8c also shows that the effects of the particles are an order of magnitude higher than the sensitivity of the test rig to excitation amplitude.

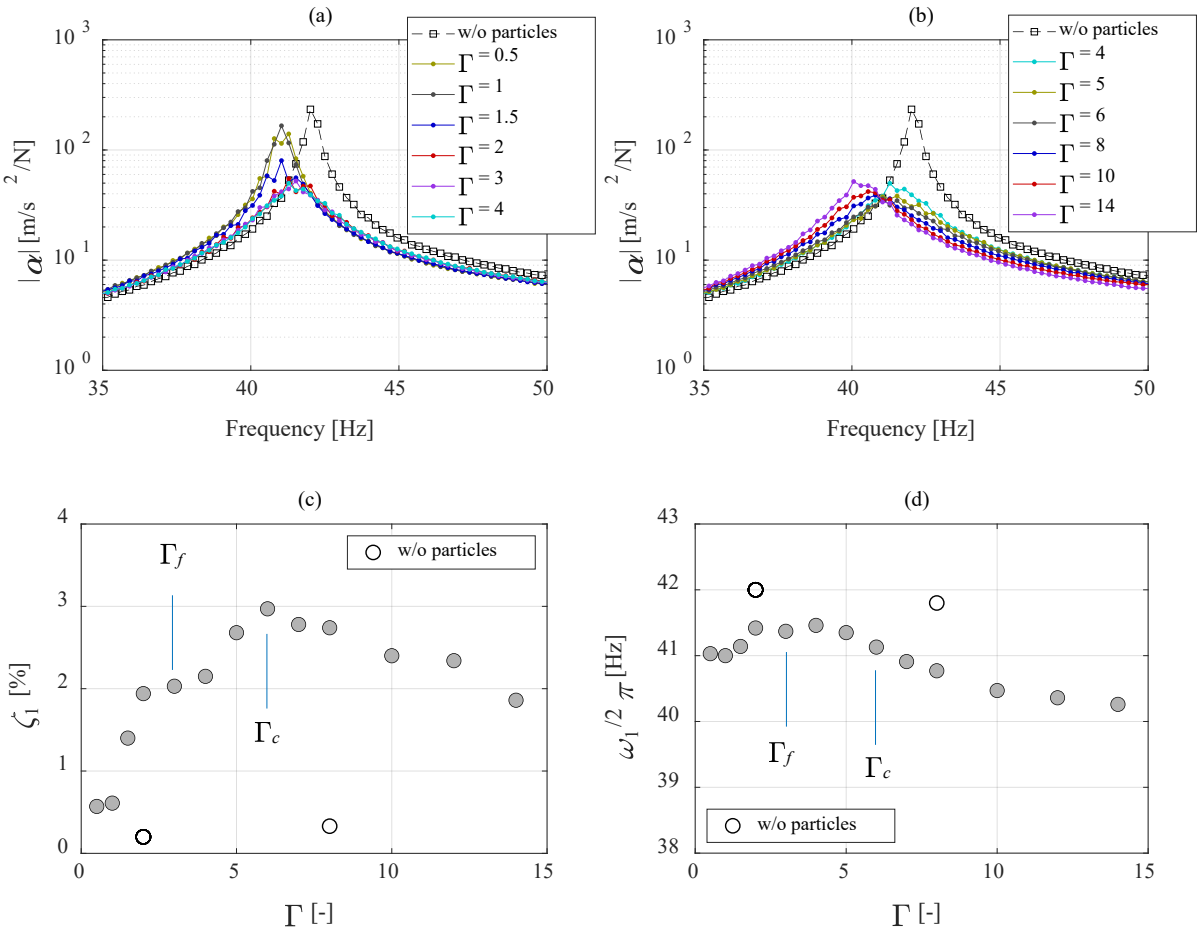

Figure 8: Experimental results for the first flexural mode of the beam (a) FRF magnitudes between Γ = 0.5 and Γ = 4, (b) FRF magnitudes between Γ = 4 and Γ = 14, (c) damping ratio, and (d) natural frequency.

It can be seen in Figure 8d that at low amplitudes (Γ = 0.5-1) the addition of particles decreases the natural frequency by an amount similar to the addition of an equivalent mass block. As the amplitude approaches the fluidisation optimum, the natural frequency recovers around half of the value lost. As the amplitude is increased further, through the two-sided collective collision optimum, the natural frequency decreases again, dropping below the low-amplitude value. Again, it is evident that the effect of the particles on the natural frequency is an order of magnitude greater than the effect of amplitude on the test rig.

The results shown here for both damping level and natural frequency are consistent with what is seen elsewhere in the literature including the following:

i. There are two optimum conditions for damping, fluidisation and two-sided collective collision. The second occurs at higher amplitude and provides more damping.

ii. During the solid-fluidisation-convection process, the particles lift away from the walls, reducing the apparent mass. Peak damping is achieved approximately midway, when most particles are fluidised. Convection reduces dissipation.

iii. Two-sided collective collision occurs when particles start to impact the second (opposite) wall in the enclosure. As the amplitude increases, the body of particles compacts together, colliding with the walls at either end, increasing the apparent mass. Changing amplitude also alters the phasing of impacts within a cycle and maximum damping is achieved at Γ_c when this is optimised [30].

Results for the higher modes are presented in the same format in Figure 9 and Figure 10.

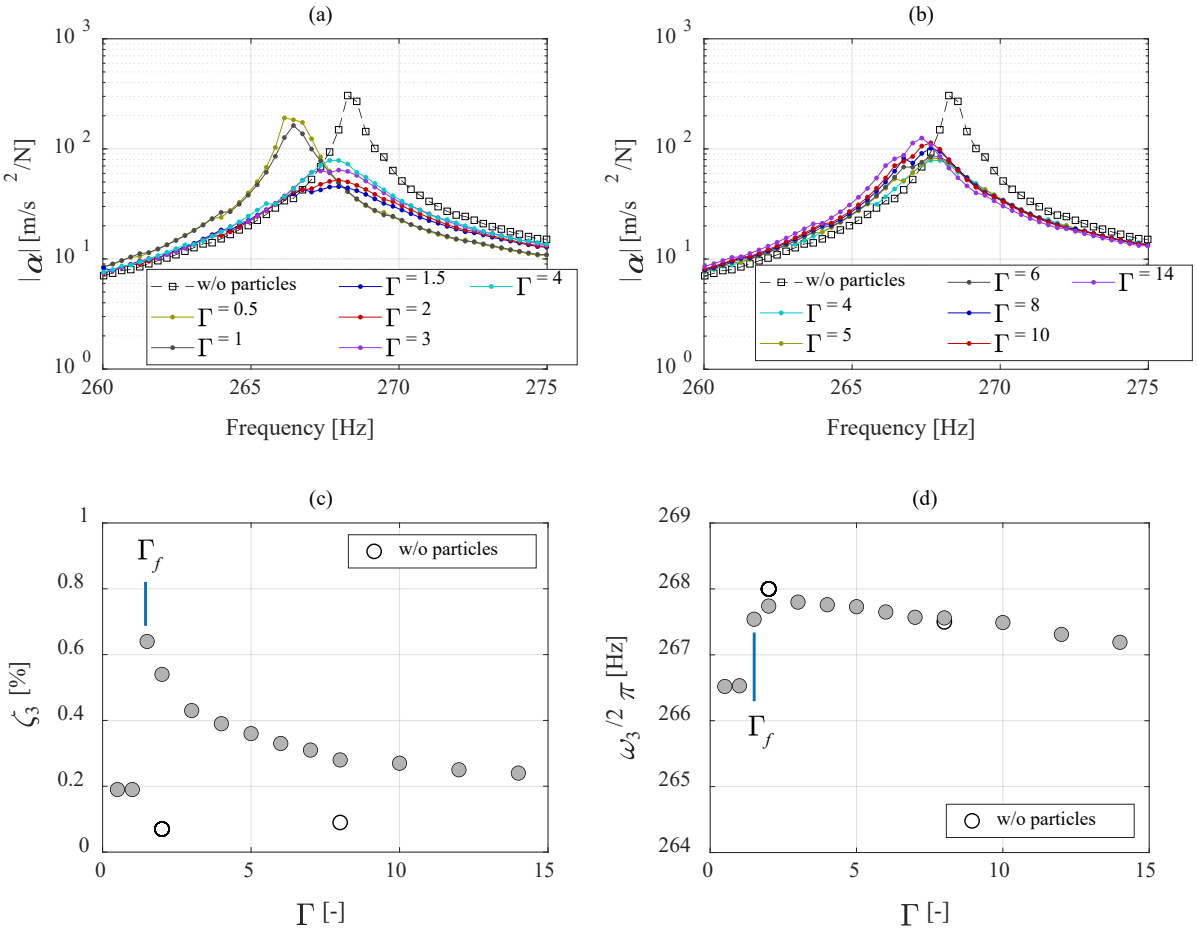

Figure 9: Experimental results for the third flexural mode of the beam (a) FRF magnitudes between $\Gamma = 0.5$ and $\Gamma = 4$, (b) FRF magnitudes between $\Gamma = 4$ and $\Gamma = 14$, (c) damping ratio, and (d) natural frequency.

While the results presented in Figure 9 and Figure 10 look somewhat different from those for the first mode, they are consistent with the expected behaviour. The key difference is that the two-sided collective collision optimum is not visible. This is because at these higher frequencies, the displacement amplitudes are much smaller for the same non-dimensional

acceleration amplitudes, so from Equation (1) for this setup, two-sided collective collision would only be observable for $\Gamma > 200$ in the third mode and $\Gamma > 1500$ in the fifth mode.

Figure 9c shows that the fluidisation optimum, Γ_f, is more apparent in the third mode than the first mode as there is no two-sided collective collision nearby for the third mode. Under these conditions, the decompaction can increase within the cavity allowing convection to become the dominant motion at higher amplitudes, decreasing damping and increasing the natural frequency. Figure 10c suggests that, at the fifth mode, Γ_f may occur at lower amplitude than the minimum investigated as the transition from solid is not clearly visible. Because the particles provide less damping and frequency change in the convection phase, the amplitude-dependent behaviour of the test rig becomes significant for the higher modes and can explain the flattening of the damping curve and the reduction in natural frequency seen at higher amplitudes in Figure 9 and Figure 10.

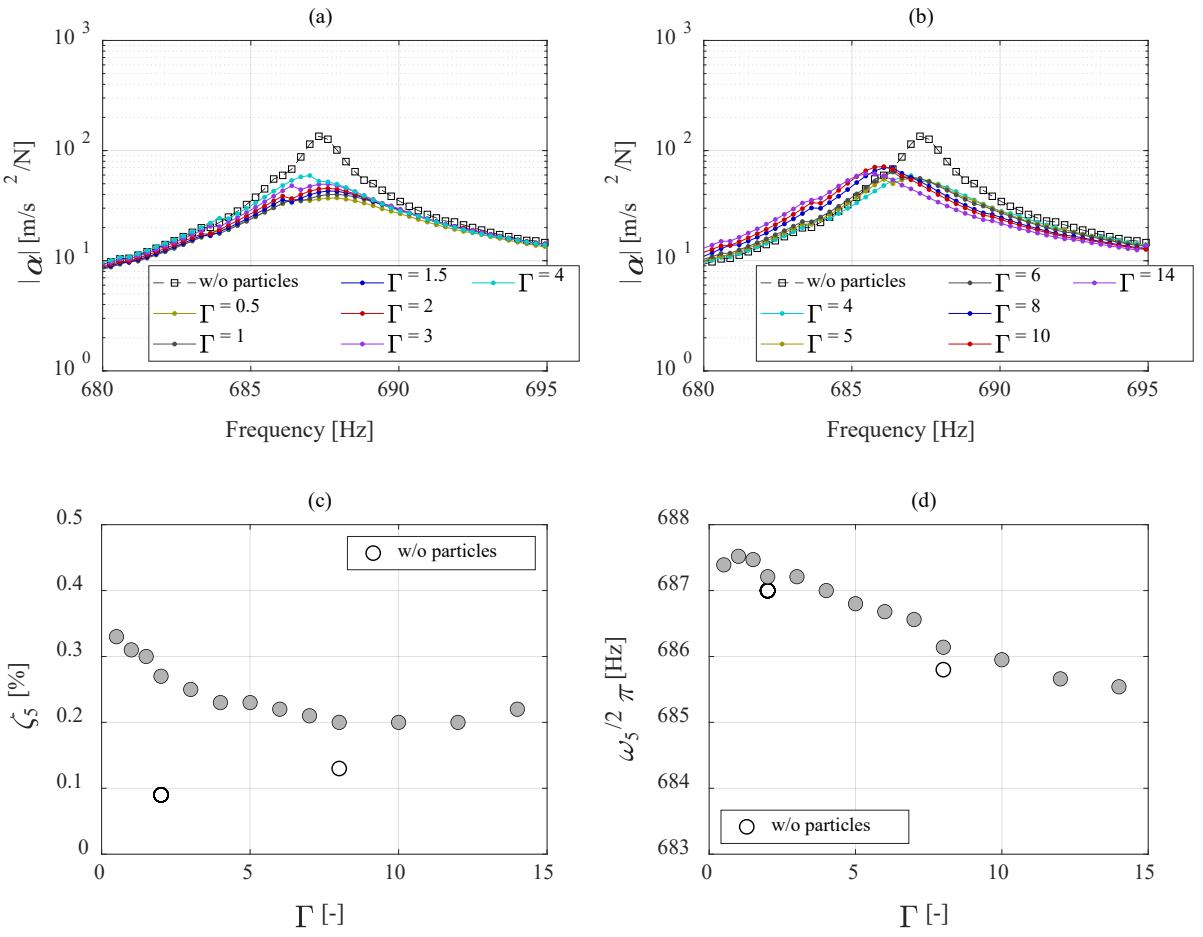

Figure 10: Experimental results for the fifth flexural mode of the beam (a) FRF magnitudes between $\Gamma = 0.5$ and $\Gamma = 4$, (b) FRF magnitudes between $\Gamma = 4$ and $\Gamma = 14$, (c) damping ratio, and (d) natural frequency.

3.2.6 Validation of the prediction method

In Figure 11, the damping ratios predicted using the method described in Section 3.1 are compared with the experimental results presented in Section 3.2.5 for all modes investigated.

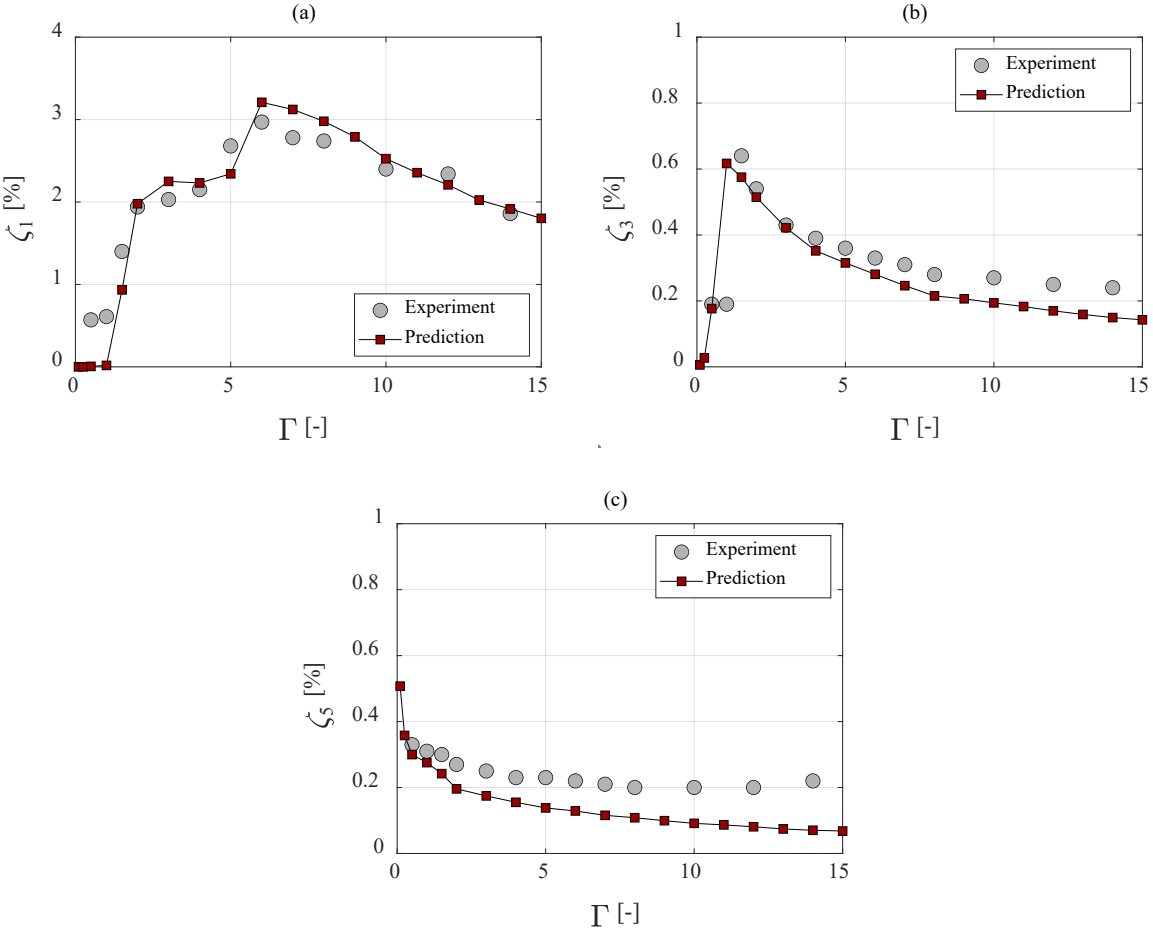

Figure 11: Comparison of damping ratio predictions with the experimental results for: (a) first, (b) third, and (c) fifth flexural modes.

It can be seen that there is a good match in terms of the overall damping ratios measured and the vibration amplitudes at which peak damping levels were achieved. Small difference can be attributed to the factors listed below.

i. The measured results include energy dissipation from friction at the clamped ends of the beam and at the fixture. While this is small (as indicated in Figure 7), it increases somewhat with amplitude, having a similar level to the size of the differences seen.

ii. DEM simulations have been observed to overestimate the energy dissipated, $\tilde{E}_{\text{dissipated},r}$ in Equation (6), by up to 20% when convection is not present and by up to 10% when it is [24,51] (see Figure 4 of the reference [24] for justification).

iii. The total mass of the particles are included as a constant mass into the FEM model when calculating the strain energy stored $E_{\text{strain},r}$ in Equation (6). However, the

apparent mass of the particles is affected by the motional behaviour changes of the granular medium [43,66,67]. This causes the underestimation of $E_{\text{strain},r}$ for the amplitudes at which the top collective collision is observed and the overestimation of $E_{\text{strain},r}$ for the amplitudes at which the fluidisation and convection motions are observed. However, this effect is likely to be small as the mass of particles is only 5% of the mass of the beam.

4 Effect of different parameters on optimum damping performance

The influence of many parameters on the fluidisation and two-sided collective collision optimums have been explained, as detailed in Table 1. There is remaining uncertainty about the effects that following parameters have:

i) Excitation frequency and sphericity on the fluidisation optimum

ii) Particle density and coefficient of restitution (CoR) on the two-sided collective collision optimum

iii) Particle elastic modulus and coefficient of friction (CoF) on both optimum conditions.

This section focuses on the determining the influence of each of these parameters on the modal damping ratios of a structure using the validated setup from Section 2. As numerical and experimental approaches were shown to deliver equivalent results, the choice of approach for each parameter is defined by convenience.

4.1 Particle sphericity

Spheroidal particle shapes (oblate, sphere and prolate) were used to investigate the effect of particle sphericity on the modal damping ratios of the beam. This work was carried out experimentally to avoid difficulties in generating some of the particle shapes in DEM [30]. Figure 12 illustrates the spheroid particle geometries investigated.

A spheroid particle geometry is obtained by revolving an ellipse around one of its principal axes (x-axis in Figure 12). Depending on the principal dimensions of ellipse (d_1 and d_2), the overall spheroid geometry can be an oblate, a sphere or a prolate as illustrated in Figure 12. A range of spheroid particle shape can be obtained by varying the principal dimensions.

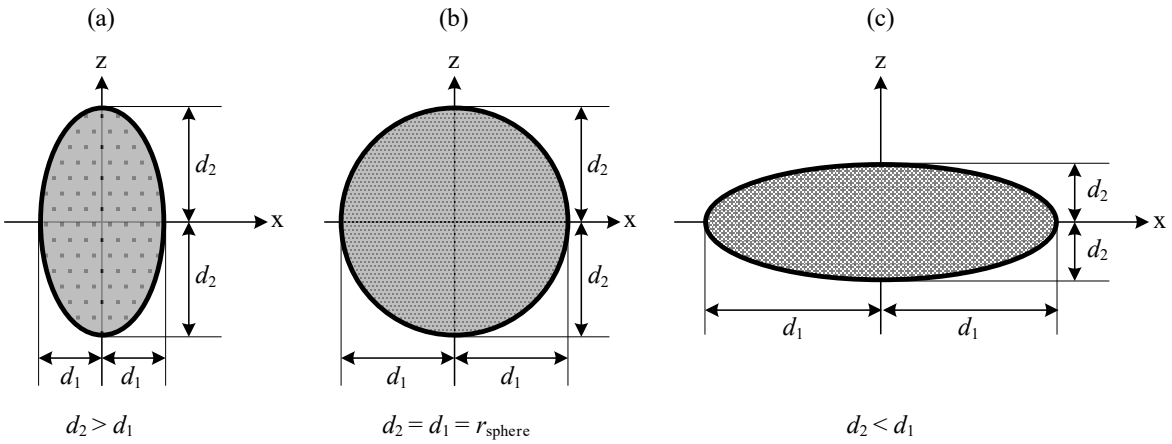

Figure 12: Spheroid particle geometries: (a) oblate, (b) sphere, and (c) prolate.

The mass of each particle shape was kept the same. Thus, the principal dimensions of spheroid geometries were related to each other with:

$$d_2 = \left(d_1 / d_2\right)^{-1/3} r_{\text{sphere}} \tag{18}$$

where r_{sphere} is the radius of the reference sphere particle.

Using r_{sphere} = 3.73 mm, a particle shape collection was obtained by manufacturing 6 different spheroidal shapes (2 oblate, 1 sphere and 3 prolate) as shown in Figure 13. The particles were made from PMMA to enable inexpensive manufacturing, to minimise magnetic interaction with the exciter, and to avoid permanent plastic deformations on particle surfaces.

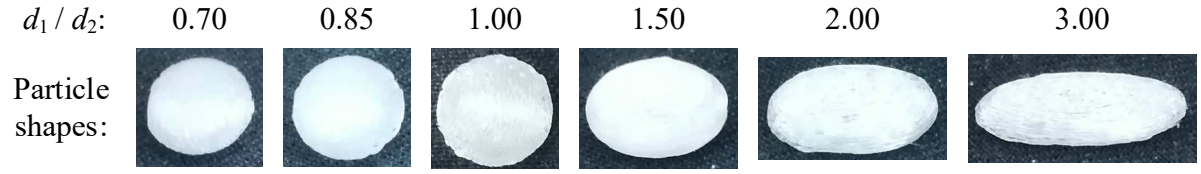

Figure 13: Spheroid particles used in experiments.

As it is visible in Figure 13, particle surfaces were not perfectly manufactured. To quantify the level of defects, a set of surface roughness measurements was conducted on the particles, d_1/d_2 = 0.70 and d_1/d_2 = 2.00. The average surface roughness of particles was found to be 12.2 μm. The relative ratio of the average surface roughness to the reference sphere diameter was about 0.16% suggesting that the overall shape would not be affected by the defects [30,45].

The influence of particle shape on the modal damping ratios of the beam structure was studied by repeating the experiments described in Section 2, replacing the spheres with the equivalent non-spherical particles. For each vibration mode investigated, the damping ratio results are set out in Figure 14.

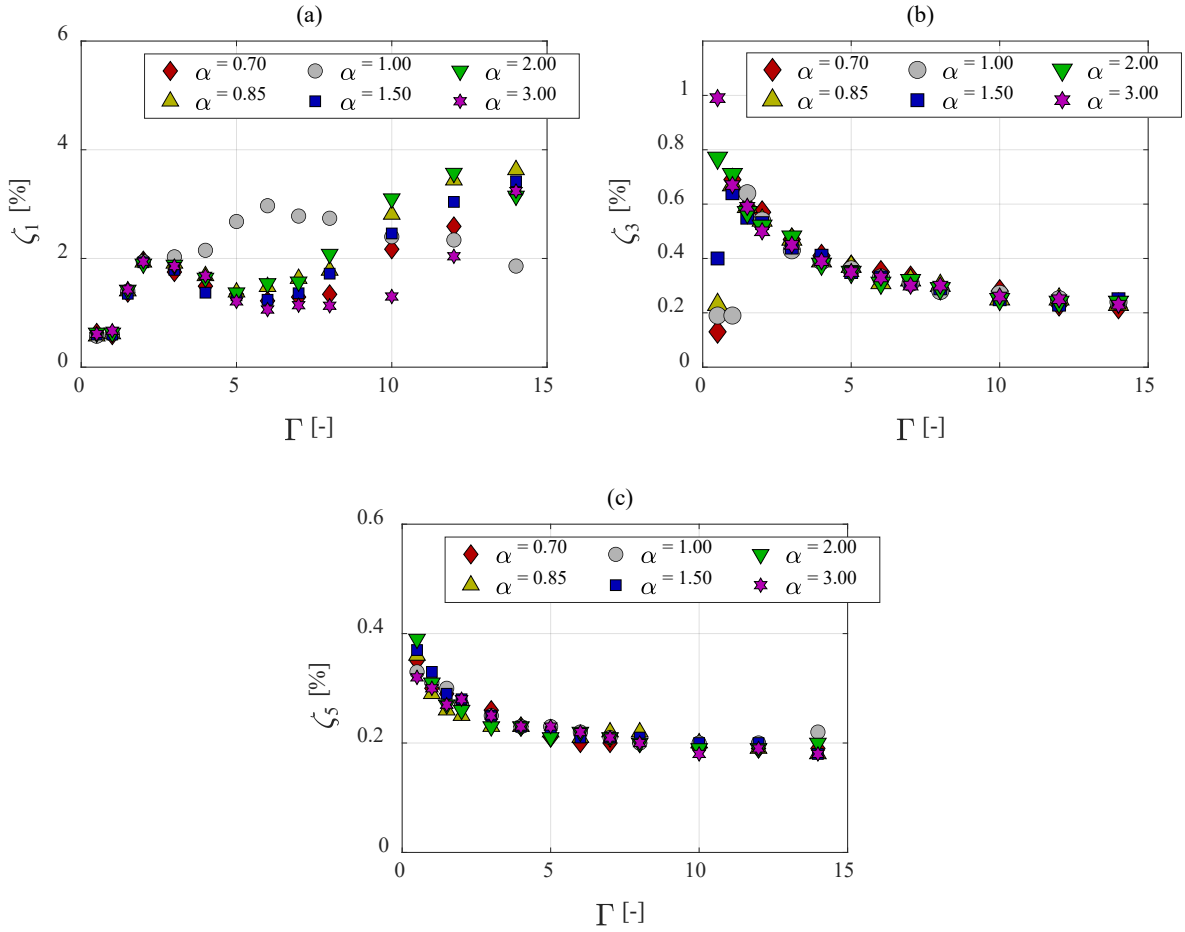

Figure 14: Effect of particle shape ($\alpha=d_1/d_2$) on the damping ratio of the structure: (a) first flexural mode, (b) third flexural mode, and (c) fifth flexural mode.

Figure 14a is the only plot showing the two-sided collective collision behaviour. The results for this motion type confirm those reported for structure-independent granular damping investigations [30] and shows that the optimum damping condition, Γ_c, occurs at higher vibration amplitudes for non-spherical particles. There are two principal causes for this that are detailed below.

i. The non-spherical particles packs more closely than the perfect spheres exhibiting less porosity in the body of particles and therefore larger clearance in the damper cavity.

ii. Significant local shear deformations occur within the particles during collective collisions with the cavity walls. To achieve collective collisions of a suitable intensity and timing within the cycles, a sufficient level of shear deformation within the particle collection is required. As rotational movement of a non-spherical particle within a compact arrangement is harder than that for an equivalent perfect sphere, the use of non-spherical particles produce a medium that is more resistant to these shear

deformations. As a result, the non-spherical particles require larger vibration amplitudes to achieve the same compactness level as the perfect spheres.

The fluidisation optimum appears in all three plots. In general, it is apparent that results for all different particle sphericity levels yield the same underlying curve. Small variations do not reveal any trends and can be attributed to uncertainty due to the random packing of particles within the enclosure cavity

This results in an important conclusion for granular damper designs – the performance of granular dampers is independent from the particle shape if the collective collision with the top wall of the cavity does not develop. It should be noted that this experimental conclusion verifies the hypothesis proposed by Sanchez et. al [53] which uses two-dimensional numerical simulations of few different particle shapes. The main explanation for this behaviour is that the particle fluidisation and convection motions are dominated by particle decompaction and at higher amplitude, subsequent transportation of particles. The shear resistance altered by particle shape does not come into play here because decompaction allows non-spherical to rotate relative to each other with ease. The major factor that controls the decompaction level and therefore can change the damping behaviour is the ratio of dynamic pressure to static pressure experienced by the particles [27,28,68,69].

4.2 Particle material

As particle material properties are hard to alter independently in a physical experiment, these comparisons were carried out using the modelling approach validated in Section 3.1. Damping levels found for the default conditions (presented in Figure 11) were obtained as changes were made to each parameter.

4.2.1 Particle density

Changing the density of particles alters the mass whilst maintaining the volume fill ratio. Figure 15 shows that the damping ratios are linearly proportional to the total mass of particles for all modes investigated and the shapes of the curves are similar. This is a well-established observation as the increase in particle density enhances energy dissipation by increasing the overall damper mass while maintaining other parameters constant. The effect on the location of the two-sided collective collision optimum (Γ_c) is minimal, whereas there appears to be a small shift in the fluidisation optimum Γ_f with lower excitation levels required to optimise systems with higher density. These results are consistent with the findings summarised in Table 1.

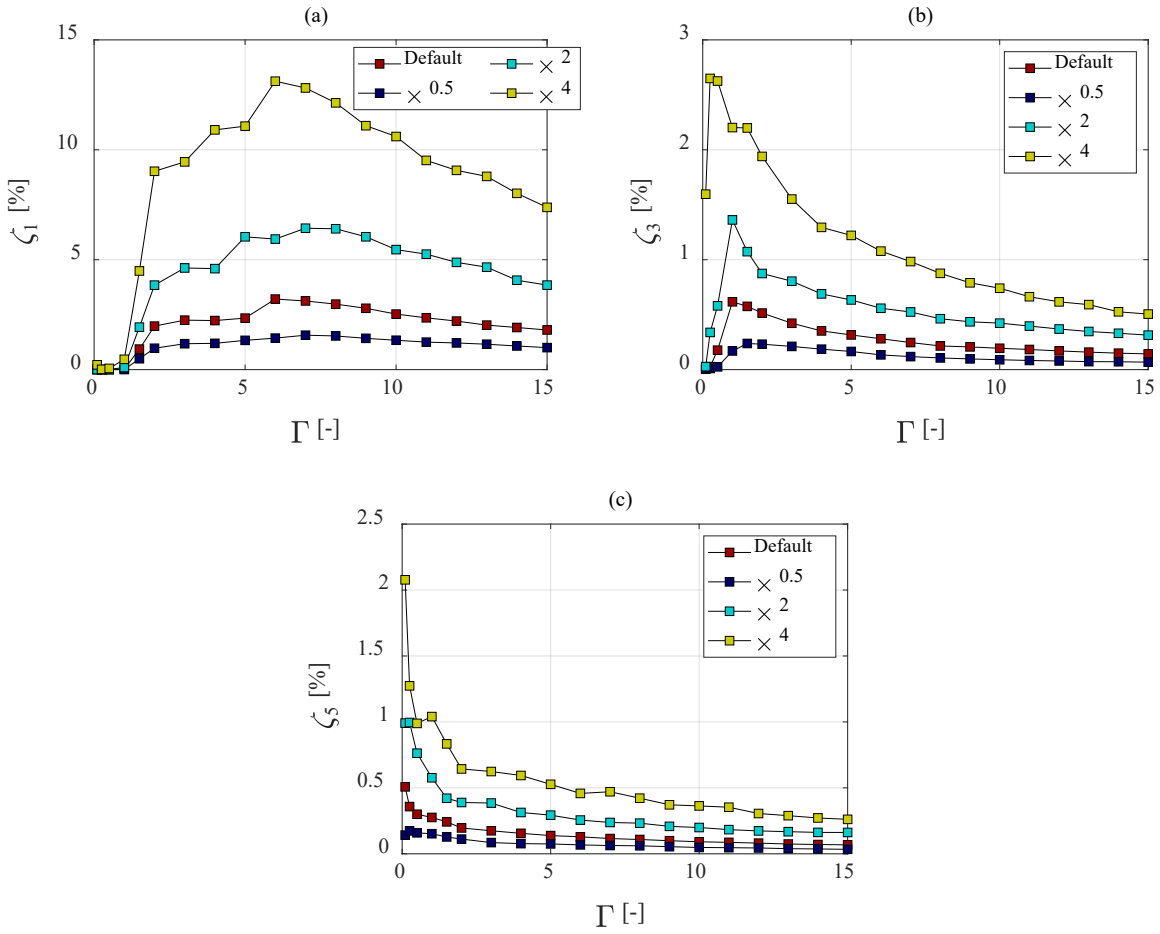

Figure 15: Sensitivity of the damping ratio to the density of particles: (a) first, (b) third, and (c) fifth modes of the beam.

4.2.2 Particle elastic modulus

Figure 16 presents the effect of particle elastic modulus on the damping of the three beam modes considered. As before, the effects on the fluidisation optimum can be seen in all three modes while the effect on the two-sided collective collision optimum can only be seen in the results for the first mode.

The results show that the excitation required to achieve optimum behaviour for both motion types is lower when the elastic modulus is low and increases with the modulus value. As elastic modulus increases, the sensitivity reduces so results for ×10 and ×100 modulus are similar. As the elastic modulus decreases, the damping ratios are higher around both optimums as a result of larger dissipative contact deformations.

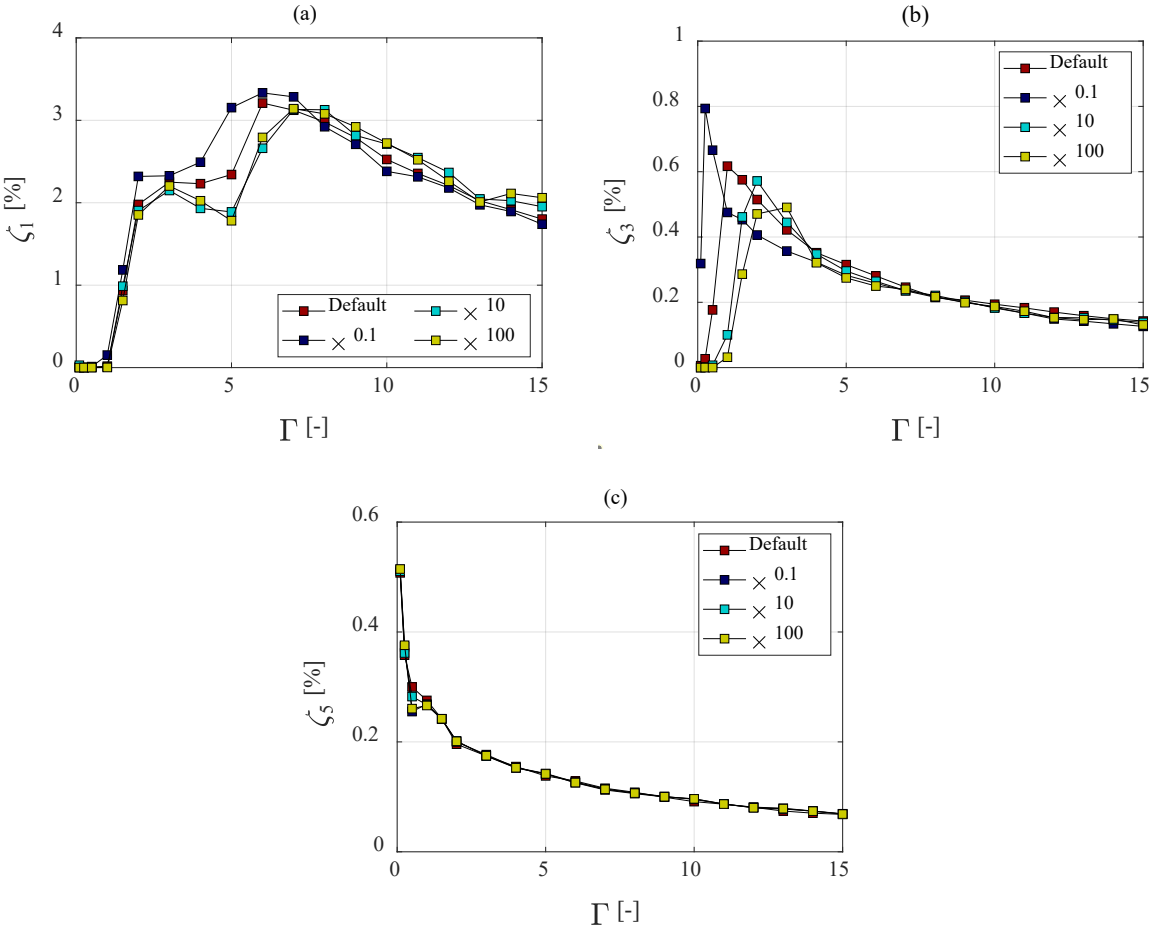

Figure 16: Sensitivity of the damping ratio to the particle elastic modulus: (a) first, (b) third, and (c) fifth modes of the beam.

4.2.3 Coefficient of restitution

The coefficient of restitution (COR) is a convenient way to describe energy loss during an impact and in this work is related to the loss factor of the particle material (low loss factor gives high CoR).

Figure 17 shows that the solid-fluidisation-convection process is not significantly affected by the CoR. This is consistent with the findings summarised in Table 1. For the collective collision optimum however, higher CoR provides more loss around the optimum. This is counter-intuitive because for a single impact, lower CoR consumes more energy, However, it has been shown elsewhere that inter-particle sliding friction is the chief dissipation mechanism [39,70,71]. It is likely that the effect of the higher CoR is to increase the number of interactions where frictional dissipation is more likely to occur.

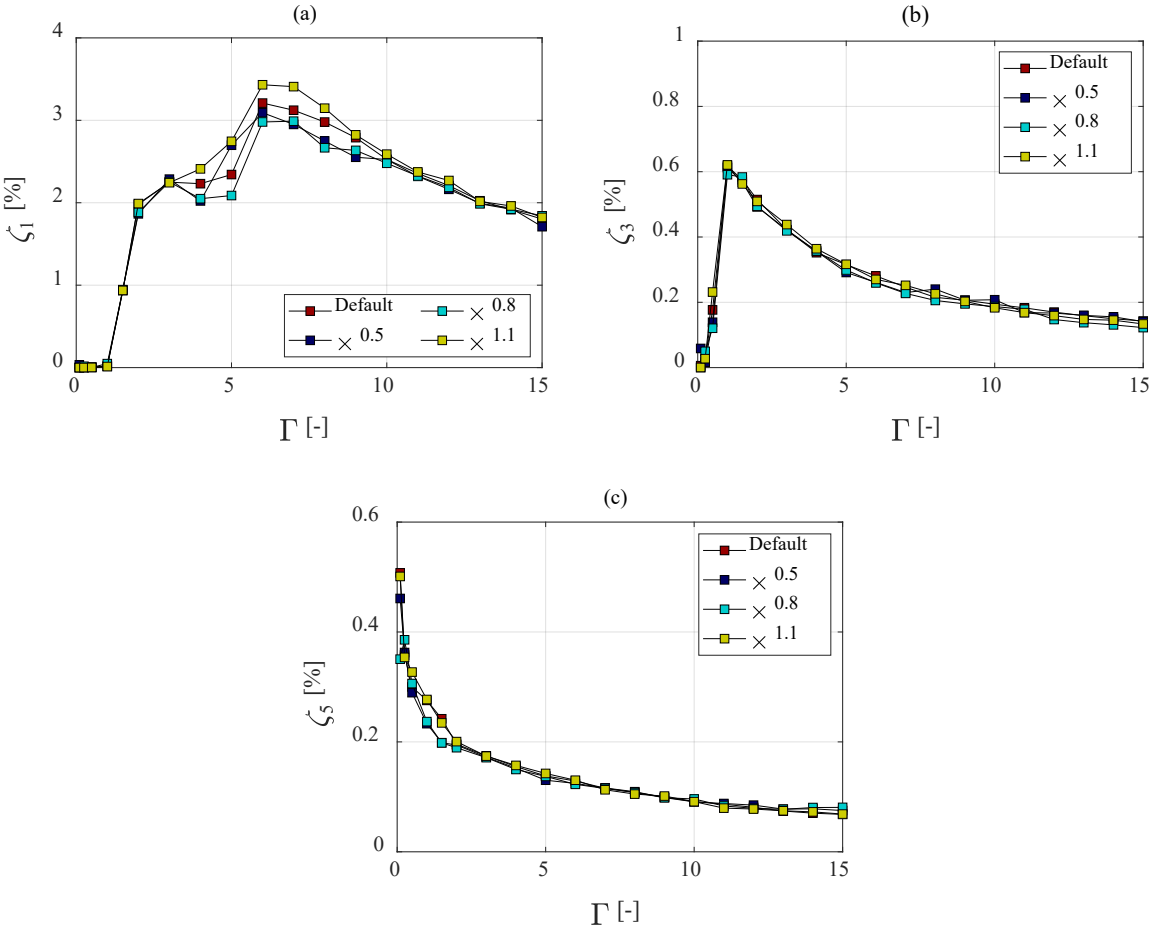

Figure 17: Sensitivity of the damping ratio to CoR: (a) first, (b) third, and (c) fifth modes of the beam.

4.2.4 Coefficient of friction

Table 1 shows that researchers have consistently found it difficult to achieve consistent results or agree on the effects of the coefficient of friction (CoF) between particles on the overall damping achieved. Results from this work are presented in Figure 18.

It is clear that the CoF affects both motion behaviour types, but in different ways. For the solid-fluidisation-convection behaviour (seen in all three modes) the effect is primarily to increase damping when moving towards the convection regime. The likely explanation is that the increase in friction retards particle transport, maintaining the fluidisation conditions at higher amplitudes. In the two-sided collective collision regime, it can be seen that reduced CoF significantly reduces damping around the optimum whereas high CoF increases it. Again, this is evidence that frictional dissipation is dominant in this regime.

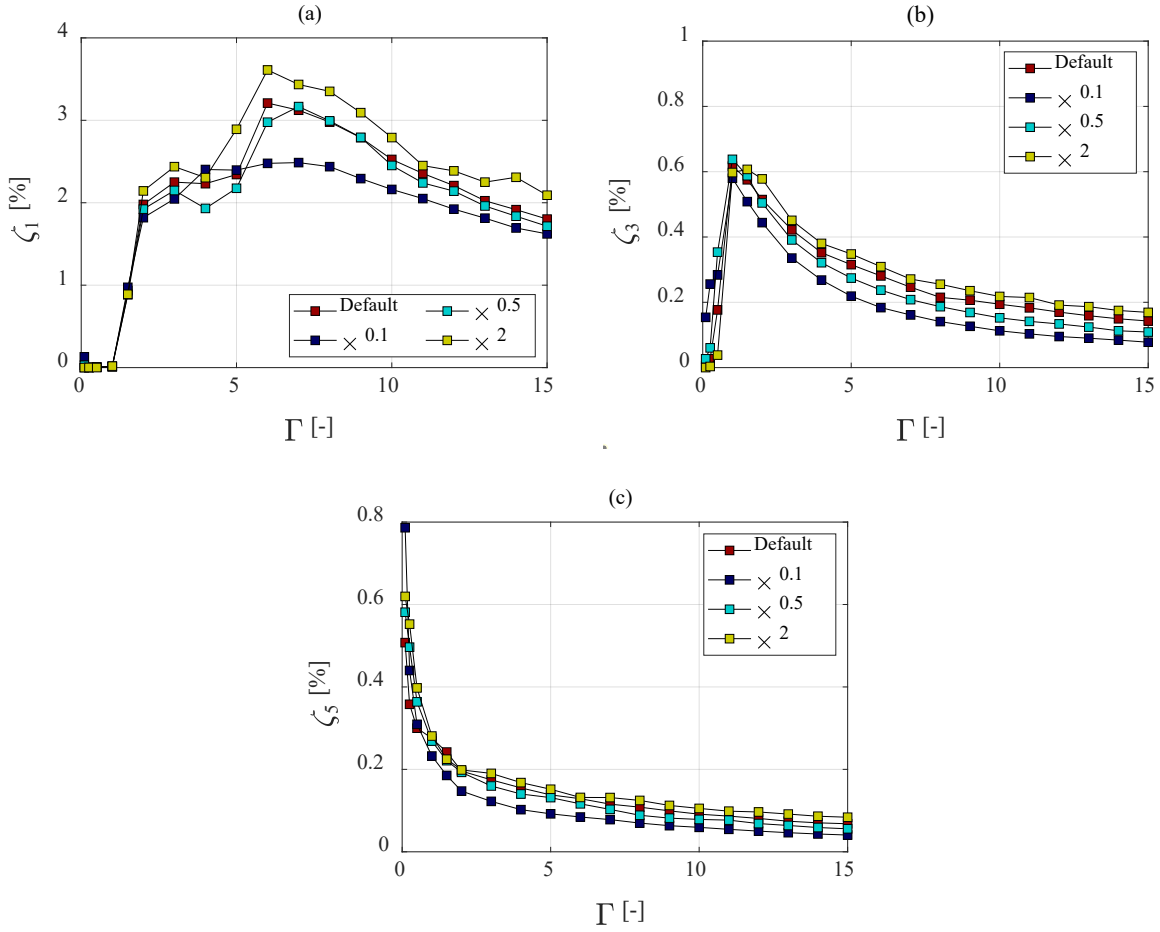

Figure 18: Sensitivity of the damping ratio to CoF: (a) first, (b) third, and (c) fifth modes of the beam.

4.3 Frequency dependency of the optimum amplitudes

The results on the three vibrational modes of the beam have shown that the amplitudes where the most effective damping can be delivered (Γ_f and Γ_c) vary depending on the natural frequency of the vibration mode considered. Also, earlier results in this section have shown that the two motional processes (solid-fluidisation-convection and two-sided collective collision) are affected differently by excitation frequency and other parameters. Because of this, it is likely that a typical damping performance curve (see Figure 11a for an example) can be decomposed into two independent curves, one for each motional process with optimum conditions at Γ_f and Γ_c respectively. This would provide significant ease in future theoretical modelling efforts for damper design purposes.

As this investigation requires many different frequencies, rather than being restricted to the vibration modes of the beam a normalised damping ratio, that maintains the characteristics of the amplitude-dependent damping ratio used earlier, was described as:

$$\zeta_{\text{normalised}}\left(\omega_e\right)=\tilde{E}_{\text{dissipated}}\left(\omega_e\right)/\left(0.5m_{\text{total}}\Gamma g/\omega_e\right)^2 \tag{19}$$

where $\tilde{E}_{\text{dissipated}}(\omega_e)$ was obtained simulating the DEM model at the excitation frequency (see Equation (14)) and m_{total} was the total mass of enclosure and particles. This calculation was repeated for a large number of frequencies from 30 to 680 Hz.

The normalised damping ratio is shown in Figure 19a for three selected excitation frequencies. It can be seen that as the excitation frequency grows, Γ_c increases significantly whilst Γ_f decreases at a lower rate. To estimate exact amplitudes at which the optimums were reached, spline interpolation was applied to the normalised damping curve with a resolution of 0.01 Hz as shown for one example in Figure 19b.

Figure 19c shows Γ_c as a function of the square of the excitation frequency, revealing a linear relationship with gradient 0.0029. As set out in Equation (1), Γ_c can be analytically estimated by considering the distance which the body of particles travels in a vibration cycle. Therefore, the gradient determined by the simulations should match with the analytical approach. Using Equation (1) and (2) gives:

$$d\Gamma_c/d\omega_e^2=4\pi^2L_{\text{enclosure}}\left(1-\upsilon/\upsilon_{\max}\right)/\left(g\pi\right) \tag{20}$$

where $L_{\text{enclosure}}$ and υ are already known from Section 3.2.1 as 0.04 m and 0.52, respectively. The value of $\upsilon_{\max}$ can be found from the sphere-packing literature considering the size of the particles used and the diameter of the cylindrical enclosure, and for this case it is 0.55 [42]. By using these numerical values, Equation (20) yields 0.0028 which is nearly identical to the gradient obtained by the simulations, confirming the expectation.

The change in Γ_f is shown as a function of the excitation frequency in Figure 19d. The optimum amplitude for this motion type appears to be linearly dependent on the excitation frequency, approaching to 3 for very low frequencies. The gradient of this linear relationship is found to be -0.0037.

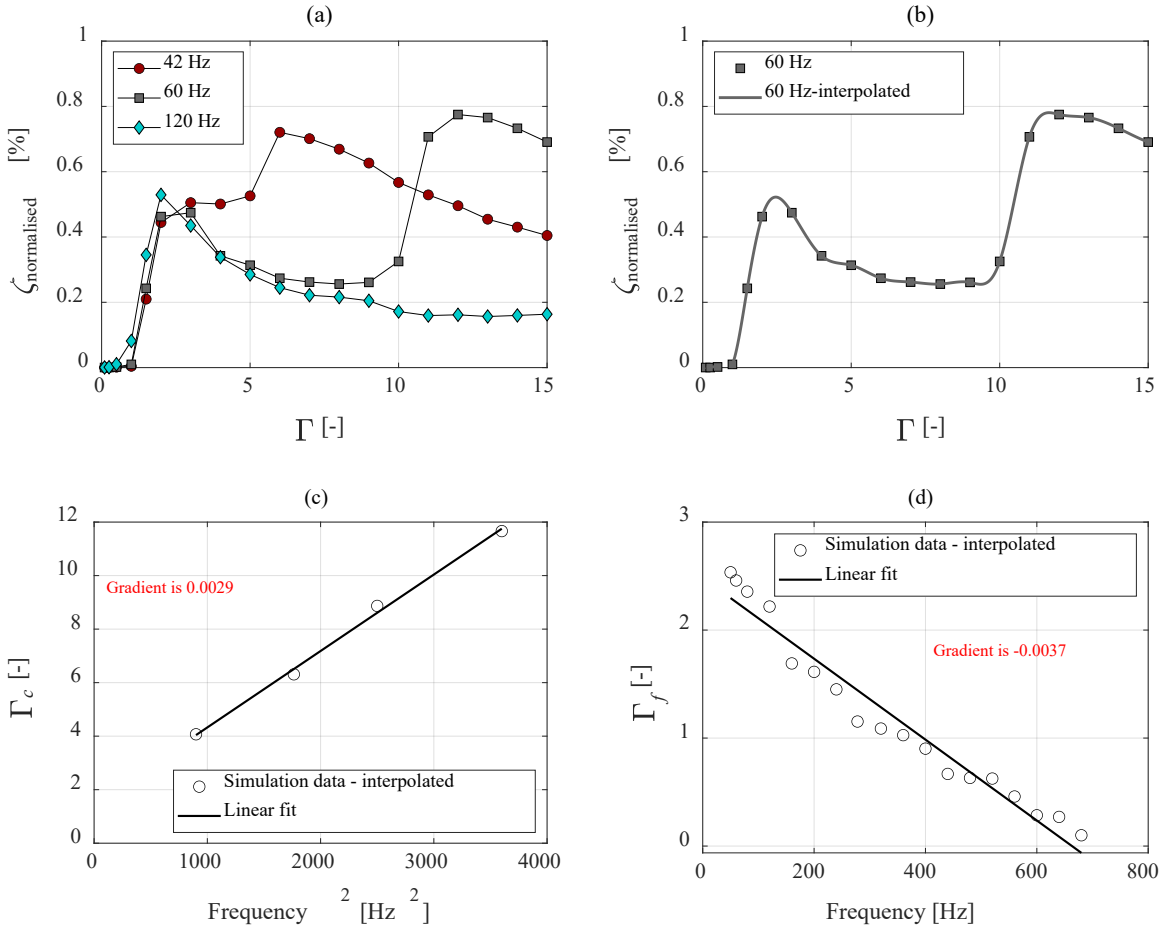

Figure 19: Frequency dependency of the optimum amplitudes: (a) the normalised damping ratio at different frequencies, (b) the normalised damping ratio at 60 Hz and its interpolated curve, (c) location of the optimum collective collision, (d) location of the fluidisation optimum.

4.4 Understanding of the two important damping processes

In addressing the lack of information about the effects of certain parameters on the performance of granular dampers, the work described in this section has provided important understanding of the nature of the two main damping processes. These are discussed below.

4.4.1 Solid-fluidisation-convection

When in the optimum fluidised condition, the granular medium goes through a compaction-decompaction process in each vibration cycle. Factors that alter the level of decompaction throughout the collection of particles are therefore those that affect damping levels. Hence bed depth (gravity-induced-pressure), compressibility and friction are significant.

The frequency dependence of this process may relate to resonance within the collection of particles. Standing waves in granular medium can typically be seen in the 500-5000 Hz range. These would result in amplification of the input vibration from the enclosure wall, so

that the true amplitude seen by most of the particles could be significantly higher. This would explain the reduction in Γ_f to below unit gravity at high frequency.

4.4.2 Two-sided collective collision

This condition arises when the excitation is sufficient to cause the particles to collide with both walls and move together as a compacted body. At optimum conditions, the end-wall collisions ensure maximum relative velocity between particle collection and the container walls. During the collision, significant shear deformation takes place within the granular medium. Factors that affect performance are therefore any that alter the timing of the wall collisions and the shear resistance of the granular medium.

5 Conclusions

The aim of this work was to provide understanding of the most important factors affecting the damping performance of a granular damper attached to a structure. This has identified two important damping processes and mapped the effects of the most common design parameters on them.

To achieve this, first the available information in the literature was collated to identify gaps in knowledge. Next a computationally-efficient predictive method for estimating the non-linear damping was developed and validated. It was shown that a modal model for the structure could be linked with damper-only results. In this work, these results were obtained from discrete element analysis, although experimental results and output from other types of damper-only models could also be used.

A damper-beam system was then used to investigate the sensitivity of the fluidisation and two-sided collective collision optimums to a variety of common parameters including excitation amplitude and frequency, particle shape, density, elastic modulus, coefficient of restitution and coefficient of friction. These results were used to complete the understanding of how to optimise granular dampers.

This paper provides a complete approach for designing granular dampers, from numerical modelling to experiments and hybrid approaches. It provides information on which factors to consider and how these will affect performance. Following this work should therefore make the task of designing a granular damper achievable for most engineers. Note that while this work is limited to applications where the motion is primarily in one translational direction, the understanding is relevant for more complex vibrational scenarios.

Appendix A

A simple analysis is carried out in this section to evaluate the significance of using real rather than complex modes to represent the structure with damper attached.

From Equations (4) and (5), noting that the acceleration amplitude of the harmonic excitation is given by A_e=Γg, the energy dissipated per cycle is written as:

$$\tilde{E}_{\text{dissipated}} = 4\epsilon\left(A_e / \omega_e\right)^2 m \tag{21}$$

The energy dissipated by an equivalent ideal viscous damper over a vibration cycle is,

$$\tilde{E}_{\text{dissipated}} = \pi c_p \omega_e \left(A_e / \omega_e^{\,2}\right)^2 \tag{22}$$

where c_p represents the equivalent viscous damping coefficient. From Equation (21) and (22), c_p is obtained as:

$$c_p = 4\epsilon m \omega_e / \pi \tag{23}$$

It should be noticed that the associated non-linearity of the granular damper is included through ϵ in the equivalent representation.

For steady-state vibrations, the dissipative harmonic forcing term arising from c_p is given by,

$$f_p = -jc_p\omega_e\left(A_e / \omega_e^{\,2}\right)e^{\mathrm{j}\omega_e t} \tag{24}$$

Replacing c_p with its expression shown in Equation (23), the dissipative forcing term becomes:

$$f_p = -\mathrm{j}4\epsilon m A_e e^{\mathrm{j}\omega_e t} / \pi \tag{25}$$

For reference, acceleration-dependent forcing of this kind is consistent with other nonlinear dampers that involve local resonators [72]. If this damper is attached to a vibrating system at a specific degree-of-freedom (DOF), its influence in the mathematical model is therefore to add the term –j4$\epsilon m/\pi$ in the relevant part of the mass matrix. This complex term in the mass matrix results in complex mode shapes in the system. The prediction method used in this paper, however, assumes real modes.

A simple way to examine the error introduced by this approximation is to analyse a 2DOF system in its even mode, where the primary oscillator represents the host system mode (without the damper), and a second mass, representing the damper, is attached to the first

mass via a spring. As the spring stiffness approaches infinity, the connection between the damper mass and the primary oscillator becomes rigid. A lower value of spring stiffness allows additional motion, as might occur when a large damper mass is attached to a flexible structure. The resulting mass and stiffness matrices of the 2 DOF system are determined by:

$$[M_{2\text{DOF}}] = m_h \begin{bmatrix} 1 & 0 \\ 0 & r_m\left(1 - j\frac{4}{\pi}\epsilon\right) \end{bmatrix} \tag{26}$$

$$[K_{2\text{DOF}}] = k_h \begin{bmatrix} 1+r_k & -r_k \\ -r_k & r_k \end{bmatrix} \tag{27}$$

where m_h and k_h are the mass and stiffness of the host system, r_m is the relative mass of the damper and r_k is the relative stiffness of the connector spring.

Figure A.1 presents results for the normalised errors in damping that arise if real modes are used instead of complex ones. In order to generate the largest expected differences, the damping efficiency was set to 1, even though this figure is rarely reached in practice. The resulting maximum modal damping ratio was 0.2 for a mass ratio of 0.32, which is significantly higher than most practical dampers. It can be seen in the figure that even under these extreme conditions, the error arising from using real modes is very small.

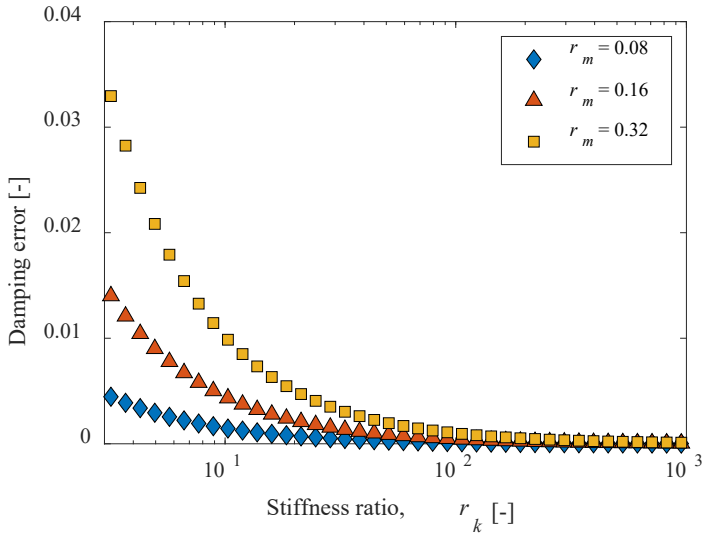

Figure A.1: Damping error arising from use of real modes rather than complex ones.

References

[1] Papalou A, Masri SF. Response of impact dampers with granular materials under random excitation. Earthq Eng Struct Dyn 1996;25:253–67. https://doi.org/10.1002/(SICI)1096-9845(199603)25:3<253::AID-EQE553>3.0.CO;2-4.

[2] Papalou A, Masri SF. Performance of particle dampers under random excitation. J Vib Acoust 1996;118:614–21. https://doi.org/10.1115/1.2888343.

[3] Lu Z, Chen X, Zhang D, Dai K. Experimental and analytical study on the performance of particle tuned mass dampers under seismic excitation. Earthq Eng Struct Dyn 2017;46:697–714. https://doi.org/10.1002/eqe.2826.

[4] Fang X, Tang J. Granular damping in forced vibration: Qualitative and quantitative analyses. J Vib Acoust 2006;128:489–500. https://doi.org/10.1115/1.2203339.

[5] Wu CJ, Liao WH, Wang MY. Modeling of granular particle damping using multiphase flow theory of gas-particle. J Vib Acoust 2004;126:196–201. https://doi.org/10.1115/1.1688763.

[6] Poschel T, Schwager T. Computational granular dynamics: models and algorithms. Berlin: Springer-Verlag; 2004.

[7] Veeramuthuvel P, Sairajan KK, Shankar K. Vibration suppression of printed circuit boards using an external particle damper. J Sound Vib 2016;366:98–116. https://doi.org/10.1016/j.jsv.2015.12.034.

[8] Ye X, Ni YQ, Sajjadi M, Wang YW, Lin CS. Physics-guided, data-refined modeling of granular material-filled particle dampers by deep transfer learning. Mech Syst Signal Process 2022;180. https://doi.org/10.1016/j.ymssp.2022.109437.

[9] Ye X, Ni YQ, Ao WK, Yuan L. Modeling of the hysteretic behavior of nonlinear particle damping by Fourier neural network with transfer learning. Mech Syst Signal Process 2024;208. https://doi.org/10.1016/j.ymssp.2023.111006.

[10] Duran J. Sands, Powders, and Grains. vol. 54. 2000.

[11] Tsuji Y, Tanaka T, Ishida T. Lagrangian numerical simulation of plug flow of cohesionless particles in a horizontal pipe. Powder Technol 1992;71:239–50. https://doi.org/10.1016/0032-5910(92)88030-L.

[12] Saeki M. Impact damping with granular materials in a horizontally vibrating system. J Sound Vib 2002;251:153–61. https://doi.org/10.1006/jsvi.2001.3985.

[13] Olson SE. An analytical particle damping model. J Sound Vib 2003;264:1155–66. https://doi.org/10.1016/S0022-460X(02)01388-3.

[14] Xu Z, Wang MY, Chen T. Particle damping for passive vibration suppression: Numerical modelling and experimental investigation. J Sound Vib 2005;279:1097–120. https://doi.org/10.1016/j.jsv.2003.11.023.

[15] Wong CX, Daniel MC, Rongong JA. Prediction of the amplitude dependent behaviour of particle dampers. AIAA/ASME/ASCE/AHS/ASC Structures, Structural Dynamics and Materials Conference, vol. 4, Honolulu, Hawaiii: 2007, p. 4167–82. https://doi.org/10.2514/6.2007-2043.

[16] Chung YC, Wu YR. Dynamic modeling of a gear transmission system containing damping particles using coupled multi-body dynamics and discrete element method. Nonlinear Dyn 2019;98:129–49. https://doi.org/10.1007/s11071-019-05177-1.

[17] Meyer N, Seifried R. Numerical and experimental investigations in the damping behavior of particle dampers attached to a vibrating structure. Comput Struct 2020;238:106281. https://doi.org/10.1016/j.compstruc.2020.106281.

[18] Duvigneau F, Koch S, Woschke E, Gabbert U. An effective vibration reduction concept for automotive applications based on granular-filled cavities. Journal of Vibration and Control 2018;24:73–82. https://doi.org/10.1177/1077546316632932.

[19] Papalou A, Masri SF. An experimental investigation of particle dampers under harmonic excitation. Journal of Vibration and Control 1998;4:361–79. https://doi.org/10.1177/107754639800400402.

[20] Panossian H V. Non-obstructive particle damping: New experiences and capabilities. 49th AIAA/ASME/ASCE/AHS/ASC Structures, Structural Dynamics and Materials Conference, Schaumburg, Illinois: 2008. https://doi.org/10.2514/6.2008-2102.

[21] Panossian H V. Structural damping enhancement via non-obstructive particle damping technique. J Vib Acoust 1992;114:101–5. https://doi.org/10.1115/1.2930221.

[22] Lu Z, Masri SF, Lu X. Studies of the performance of particle dampers attached to a two-degrees-of-freedom system under random excitation. Journal of Vibration and Control 2011;17:1454–71. https://doi.org/10.1177/1077546310370687.

[23] Ehrgott R, Panossian H V., Davis G. Modeling techniques for evaluating the effectiveness of particle damping in turbomachinery. AIAA/ASME/ASCE/AHS/ASC Structures, Structural Dynamics and Materials Conference, Palm Springs, California: 2009. https://doi.org/10.2514/6.2009-2690.

[24] Terzioglu F, Rongong JA, Lord CE. Motional phase maps for estimating the effectiveness of granular dampers. Mech Syst Signal Process 2023;188:110038. https://doi.org/10.1016/j.ymssp.2022.110038.

[25] Meyer N, Seifried R. Toward a design methodology for particle dampers by analyzing their energy dissipation. Comput Part Mech 2020. https://doi.org/10.1007/s40571-020-00363-0.

[26] Meyer N, Seifried R. Systematic design of particle dampers for transient vertical vibrations. Granul Matter 2023;25. https://doi.org/10.1007/s10035-022-01290-y.

[27] Liu W, Tomlinson GR, Rongong JA. The dynamic characterisation of disk geometry particle dampers. J Sound Vib 2005;280:849–61. https://doi.org/10.1016/j.jsv.2003.12.047.

[28] Ben Romdhane M, Bouhaddi N, Trigui M, Foltête E, Haddar M. The loss factor experimental characterisation of the non-obstructive particles damping approach. Mech Syst Signal Process 2013;38:585–600. https://doi.org/10.1016/j.ymssp.2013.02.006.

[29] Zhang K, Chen T, Wang X, Fang J. Rheology behavior and optimal damping effect of granular particles in a non-obstructive particle damper. J Sound Vib 2016;364:30–43. https://doi.org/10.1016/j.jsv.2015.11.006.

[30] Terzioglu F, Rongong JA, Lord CE. Influence of particle sphericity on granular dampers operating in the bouncing bed motional phase. J Sound Vib 2023;554:117690. https://doi.org/10.1016/j.jsv.2023.117690.

[31] Terzioglu F, Rongong JA, Lord CE. The dissipative characteristics of oblate particles in granular dampers. Proceedings of the International Conference on Structural Dynamic , EURODYN, vol. 2, 2020, p. 4851–66. https://doi.org/10.47964/1120.9393.20452.

[32] Sack A, Heckel M, Kollmer JE, Zimber F, Pöschel T. Energy dissipation in driven granular matter in the absence of gravity. Phys Rev Lett 2013;111:1–5. https://doi.org/10.1103/PhysRevLett.111.018001.

[33] Sack A, Windows-Yule K, Heckel M, Werner D, Pöschel T. Granular dampers in microgravity: sharp transition between modes of operation. Granul Matter 2020;22:1–6. https://doi.org/10.1007/s10035-020-01017-x.

[34] Yao B, Chen Q. Investigation on zero-gravity behavior of particle dampers. Journal of Vibration and Control 2015;21:124–33. https://doi.org/10.1177/1077546313488157.

[35] Eshuis P, van der Weele K, van der Meer D, Bos R, Lohse D. Phase diagram of vertically shaken granular matter. Physics of Fluids 2007;19. https://doi.org/10.1063/1.2815745.

[36] Zhang K, Zhong H, Kou F, Chen Y, Gao Y. Dissipation behaviors of suspended granular balls in a vibrated closed container. Powder Technol 2022;399:117158. https://doi.org/10.1016/j.powtec.2022.117158.

[37] Yin Z, Su F, Zhang H. Investigation of the energy dissipation of different rheology behaviors in a non-obstructive particle damper. Powder Technol 2017;321:270–5. https://doi.org/10.1016/j.powtec.2017.07.090.

[38] Zhang K, Zhong H, Chen T, Kou F, Chen Y, Bai C. Dissipation behaviors of granular balls in a shaken closed container. Mech Syst Signal Process 2022;172:108986. https://doi.org/10.1016/j.ymssp.2022.108986.

[39] Terzioglu F, Rongong JA, Lord CE. Construction of motional phase maps for granular dampers. Internoise 2022 - 51st International Congress and Exposition on Noise Control Engineering 2022;265:128–39. https://doi.org/10.3397/in_2022_0025.

[40] Darabi B, Rongong JA. Polymeric particle dampers under steady-state vertical vibrations. J Sound Vib 2012;331:3304–16. https://doi.org/10.1016/j.jsv.2012.03.005.

[41] Zamponi F. Mathematical physics: Packings close and loose. Nature 2008;453:606–7. https://doi.org/10.1038/453606a.

[42] McGEARY RK. Mechanical packing of spherical particles. Journal of the American Ceramic Society 1961;44:513–22. https://doi.org/10.1111/j.1151-2916.1961.tb13716.x.

[43] Masmoudi M, Job S, Abbes MS, Tawfiq I, Haddar M. Experimental and numerical investigations of dissipation mechanisms in particle dampers. Granul Matter 2016;18:1–11. https://doi.org/10.1007/s10035-016-0667-4.

[44] Darabi B, Rongong JA, Zhang T. Viscoelastic granular dampers under low-amplitude vibration. Journal of Vibration and Control 2018;24:708–21. https://doi.org/10.1177/1077546316650098.

[45] Terzioglu F, Rongong JA, Lord CE. The effect of particle surface roughness on granular energy dissipation performance. Proceedings of the International Congress on Acoustics, Gyeongju, South Korea: 2022.

[46] Bannerman MN, Kollmer JE, Sack A, Heckel M, Mueller P, Pöschel T. Movers and shakers: Granular damping in microgravity. Phys Rev E 2011;84:1–9. https://doi.org/10.1103/PhysRevE.84.011301.

[47] Wong C, Rongong J. Control of particle damper nonlinearity. AIAA Journal 2009;47:953–60. https://doi.org/10.2514/1.38795.

[48] Lu Z, Masri SF, Lu X. Parametric studies of the performance of particle dampers under harmonic excitation. Struct Control Health Monit 2011;18:79–98. https://doi.org/10.1002/stc.359.

[49] Lu Z, Lu X, Masri SF. Studies of the performance of particle dampers under dynamic loads. J Sound Vib 2010;329:5415–33. https://doi.org/10.1016/j.jsv.2010.06.027.

[50] Marhadi KS, Kinra VK. Particle impact damping: Effect of mass ratio, material, and shape. J Sound Vib 2005;283:433–48. https://doi.org/10.1016/j.jsv.2004.04.013.

[51] Wong CX, Daniel MC, Rongong JA. Energy dissipation prediction of particle dampers. J Sound Vib 2009;319:91–118. https://doi.org/10.1016/j.jsv.2008.06.027.

[52] Sánchez M, Rosenthal G, Pugnaloni LA. Universal response of optimal granular damping devices. J Sound Vib 2012;331:4389–94. https://doi.org/10.1016/j.jsv.2012.05.001.

[53] Sánchez M, Carlevaro CM, Pugnaloni LA. Effect of particle shape and fragmentation on the response of particle dampers. Journal of Vibration and Control 2014;20:1846–54. https://doi.org/10.1177/1077546313480544.

[54] Hughes TJR. The Finite Element Method: Linear Static and Dynamic Finite Element Analysis. vol. 65. New York: Dover Publications; 2000. https://doi.org/620/.001/51535.

[55] Inman DJ. Engineering vibration. New Jersey: Pearson; 2014.

[56] Cundall PA, Strack ODL. A discrete numerical model for granular assemblies. Geotechnique 1979;29:47–65. https://doi.org/10.1680/geot.1979.29.1.47.

[57] Stronge WJ. Impact Mechanics. Second. New York: Cambridge University Press; 2018.

[58] Fowler BL, Flint EM, Olson SE. Effectiveness and predictability of particle damping. Proc. SPIE 3989, Smart Structures and Materials 2000: Damping and Isolation, vol. 3989, Newport Beach, California: 2000, p. 356–67. https://doi.org/10.1117/12.384576.

[59] Saeki M. Analytical study of multi-particle damping. J Sound Vib 2005;281:1133–44. https://doi.org/10.1016/j.jsv.2004.02.034.

[60] Fang X, Tang J, Luo H. Granular damping analysis using an improved discrete element approach. J Sound Vib 2007;308:112–31. https://doi.org/10.1016/j.jsv.2007.07.034.

[61] Duan Y, Chen Q. Simulation and experimental investigation on dissipative properties of particle dampers. Journal of Vibration and Control 2011;17:777–88. https://doi.org/10.1177/1077546309356183.

[62] Ansys. Academic Research Mechanical, 2022 R2 2022.

[63] Altair Engineering Inc. EDEM 2021.1 2021.

[64] Di Renzo A, Di Maio FP. Comparison of contact-force models for the simulation of collisions in DEM-based granular flow codes. Chem Eng Sci 2004;59:525–41. https://doi.org/10.1016/j.ces.2003.09.037.

[65] Ewins DJ. Modal testing : theory, practice, and application. Hertfordshire: Research Studies Press; 2000.

[66] Sánchez M, Pugnaloni LA. Effective mass overshoot in single degree of freedom mechanical systems with a particle damper. J Sound Vib 2011;330:5812–9. https://doi.org/10.1016/j.jsv.2011.07.016.

[67] Ferreyra MV, Baldini M, Pugnaloni LA, Job S. Effect of lateral confinement on the apparent mass of granular dampers. Granul Matter 2021;23. https://doi.org/10.1007/s10035-021-01090-w.

[68] Bajkowski JM, Dyniewicz B, Gębik-Wrona M, Bajkowski J, Bajer CI. Reduction of the vibration amplitudes of a harmonically excited sandwich beam with controllable core. Mech Syst Signal Process 2019;129:54–69. https://doi.org/10.1016/j.ymssp.2019.04.024.

[69] Bajkowski JM, Dyniewicz B, Bajer CI. Damping properties of a beam with vacuum-packed granular damper. J Sound Vib 2015;341:74–85. https://doi.org/10.1016/j.jsv.2014.12.036.

[70] Mao K, Wang MY, Xu ZZ, Chen T. Simulation and characterization of particle damping in transient vibrations. J Vib Acoust 2004;126:202–11. https://doi.org/10.1115/1.1687401.

[71] Mao K, Wang MY, Xu Z, Chen T. DEM simulation of particle damping. Powder Technol 2004;142:154–65. https://doi.org/10.1016/j.powtec.2004.04.031.

[72] Zhao B, Thomsen HR, Pu X, Fang S, Lai Z, Damme B Van, et al. A nonlinear damped metamaterial: Wideband attenuation with nonlinear bandgap and modal dissipation. Mech Syst Signal Process 2024;208. https://doi.org/10.1016/j.ymssp.2023.111079.